A Pseudodecoupled Modeling and Analysis Method for Interleaved Multiphase Converters With Coupled Inductors

Li Wei, *Member, IEEE*, Bingqi Ouyang, *Member, IEEE*, and Yanbo Liu, *Graduate Student Member, IEEE*

***Abstract*—Interleaved multiphase converters with coupled inductors (MCCIs), which can increase the power density of switching power supplies, is a research hotspot in power electronics. However, it is difficult to obtain ideal symmetrical coupled inductors due to manufacturing inaccuracies, especially in high-power applications. Asymmetrical coupling of inductors will lead to phase imbalance in MCCIs and difficulty in circuit analysis. To address this, this article proposes a novel modeling method for MCCIs, extendable to the analysis of interleaved multiphase converters with asymmetrical coupled inductors. This helps to simplify the analysis of MCCIs and allows easier and more efficient controller and inductor design for MCCIs. First, the concept of pseudodecoupled equivalent circuits for MCCIs is presented, which solves the problem of modeling MCCIs. Second, the transient behavior and steady-state current ripple performance of MCCIs are analyzed based on the pseudodecoupled method. Third, the effect of the degree of inductance asymmetry on the MCCI performance is quantitatively analyzed. Then, the feasibility of extending PWM phase sequence and phase-shift adjustment methods to MCCIs is further verified using the proposed modeling approach, which can reduce the current ripple. Finally, the accuracy of the modeling and analysis methods is verified by simulation and experiment.**

***Index Terms*—Asymmetrical coupled inductor, current ripple, high-power multiphase converter, pseudodecoupled equivalent circuit, PWM phase shift and phase sequence, transient response.**

I. Introduction

REDUCING the volume of passive components is one of the key methods to improve the power density of converters, especially in high-power applications [1], [2], [3], [4], [5]. For example, the magnetic components and filter capacitors in a 300-kW boost converter for fuel cell vehicle applications may account for 30% and 15% of the converter volume, respectively. The use of coupled inductors in interleaved multiphase converters can not only reduce the size of the magnetic components, but also improve the dynamic performance and reduce the current ripple, which will cut down the size of the capacitors [6], [7], [8], [9]. However, it is impossible to avoid asymmetrical coupling of inductors due to manufacturing reasons, especially for high-power applications. For example, a ladder-core structure [10], [11] with three rungs is usually adopted for the three-phase coupled inductor in a 150-kW boost converter. Theoretically, the cross-sectional area of each rung should be different to make sure of the symmetrical coupling. However, the customized magnetic core not only lacks cost-effectiveness, but also exhibits low accuracy. Thus, in practical applications, a ladder-core structure with the same cross-sectional area of each rung is adopted as a simplified alternative. This will inevitably lead to the asymmetrical coupling of inductors and phase imbalance of the converter resulting in difficulties in the transient and ripple analysis of the circuit [12], [13]. Indirect coupling [14], [15] and lateral coupling [16] can be used to ensure symmetrical coupling to some extent and reduce cost. However, for high-power applications, the feasibility of these coupled inductors and their advantages in terms of power density still need to be discussed. Therefore, there is a critical need for an analytical method suitable for multiphase converters with asymmetrical coupled inductors (MCACIs).

Currently, there are analytical methods for multiphase converters with symmetrical coupled inductors. Wong et al. [17] were the first to suggest that coupled inductors can be used to improve the performance of multiphase converters. They analyzed how the converter performance varies with the coupling coefficient and duty cycle based on a coupled inductor matrix model of a two-phase buck converter with symmetrical assumption. They introduced the parameters of steady-state equivalent inductance and transient equivalent inductance which are used to describe the behavior of coupled inductors and calculate the dynamic response and steady-state ripple performances of the converter. Dong [18] further explored this approach in the analysis of an n-phase parallel buck converter with coupled inductors. Zhou et al. [20], [21] employed the inductance-dual model of coupled inductors to analyze the n-phase parallel buck converter with coupled inductors, which offered opportunities to further study the details of core loss, saturation, and flux distribution in the core. However, those analytical methods are not suitable for MCACIs.

Received 16 July 2024; revised 16 November 2024; accepted 22 December 2024. Date of publication 7 January 2025; date of current version 26 February 2025. This work was supported in part by the Pudong District Science and Technology Development Fund under Grant PKX2022-w03. Recommended for publication by Associate Editor Carl N.M. Ho. *(Corresponding author: Bingqi Ouyang.)*

The authors are with the Department of Electrical Engineering, Tongji University, Shanghai 201804, China (e-mail: weili@tongji.edu.cn; bingqi@tongji.edu.cn; 2230674@tongji.edu.cn).

Color versions of one or more figures in this article are available at https://doi.org/10.1109/TPEL.2025.3526618.

Digital Object Identifier 10.1109/TPEL.2025.3526618

Currently, there are relatively few studies on MCACIs. The difficulty in analyzing MCACIs is that it not only has more parameters, but also the current ripple is related to both PWM phase shift and phase sequence [22]. In [18], the performance of a three-phase buck converter with an asymmetrical coupled inductor was discussed by an exhaustive method, and in [19] this methodology is further analyzed and experimentally verified in detail. Based on this method, researchers have written automated programs to calculate steady-state equivalent inductance and transient equivalent inductance of n-phase coupled inductor buck converters considering asymmetric designs, where each phase's PWM stage is sequentially phase-shifted by $2\pi/n$ [23]. However, the above method is not a general solution for analyzing MCACIs, and the relationship among current ripple, PWM phase shift and phase sequence is not discussed. Therefore, a more general method is needed to quantitatively analyze the performance of MCACIs. Quantifying the relationship among current ripple, PWM phase shift and phase sequence is also a worthwhile research problem, because minimizing the current ripple is an effective way to reduce the filter capacitance and increase the reliability of converters [24], [25]. There are some studies on current ripple optimization through changing PWM phase shift and phase sequence for multiphase asymmetrical converters with independent inductors [26], [27], [28], though. It is still rare to find such studies in MCACIs.

The motivation of this article is to develop a generalized modeling method for interleaved multiphase converters with coupled inductors (MCCIs), extendable to the analysis of MCACIs, in order to analyze analyzing the impact of multiphase coupled inductors on the transient behavior and ripple current of the converter efficiently and quantitatively. The theoretical framework of modeling MCCIs is described with the concept of pseudodecoupled equivalent circuits. The pseudodecoupling modeling method first constructs a diagonal matrix without coupling relationship based on the original inductance matrix of the multiphase coupled inductors, and then uses the proposed ripple distribution coefficient matrix to describe the coupling relationship between the inductors, which can simplify the analysis of MCCIs as an independent inductor converter. With the proposed methodology, the relationship among ripple current, PWM phase shift and phase sequence can be easily calculated allowing for the further control strategy optimization of MCACIs.

The rest of this article is organized as follows. Section II describes the proposed pseudodecoupled modeling method for MCCIs and analyzes the transient performance and steady-state current ripple performance of MCCIs based on this modeling method. Section III quantitatively analyzes the effect of the degree of inductance asymmetry on the performance of the MCCI and gives the suggestion of asymmetrical coupled inductors compensating design and coupling coefficients selection. Section IV verifies the idea of extending the PWM phase sequence and phase shift optimization method to MCCIs, and illustrates the optimization idea with a case study. In Section V, with a six-phase Boost converter, the accuracy and feasibility of the proposed model, analysis method and PWM phase sequence and phase shift optimization method are verified from simulation and experiment. Finally, Section VI concludes this article.

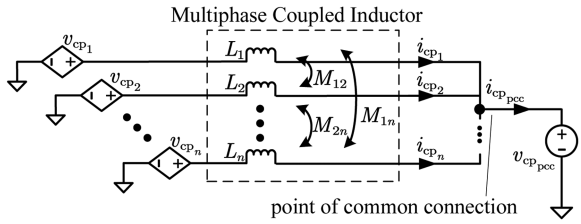

Fig. 1. Equivalent circuit of an interleaved multiphase converter with coupled inductors.

II. Proposed Modeling Method for Multiphase Converters With Asymmetrical Coupled Inductors

In this section, a method is proposed to address the dynamic and steady-state performance analysis issues of MCCIs with n phases and a switching frequency of f_{sw}, applicable to both symmetrical and asymmetrical inductors. The equivalent circuit is illustrated in Fig. 1, where the inductor's equivalent series resistance is neglected. This equivalent circuit is a generalized topology that can represent multiphase Buck converters, multiphase Boost converters and other topologies with similar structures. For instance, for a buck converter, the voltage source v_{pcc} represents the equivalent model of the load and output filter, and controlled voltage sources v_1, v_2,... v_n denote the equivalent models of the inputs of each phase. While for a boost converter, the voltage source v_{pcc} stands for the equivalent model of its input source and input filter, and controlled voltage sources v_1, v_2,... v_n represent the equivalent models of the output of each phase. The phase voltages and phase currents in the MCCI are described by the inductance matrix $\mathbf{L}$

$$\underbrace{\begin{bmatrix} v_{cp_1} - v_{cp_{pcc}} \\ v_{cp_2} - v_{cp_{pcc}} \\ \vdots \\ v_{cp_n} - v_{cp_{pcc}} \end{bmatrix}}_{\mathbf{V_{cp}}} = \underbrace{\begin{bmatrix} L_1 & M_{12} & \cdots & M_{1n} \\ M_{21} & L_2 & \cdots & M_{2n} \\ \vdots & \vdots & \ddots & \vdots \\ M_{n1} & M_{n2} & \cdots & L_n \end{bmatrix}}_{\mathbf{L}} \underbrace{\begin{bmatrix} di_{cp_1}/dt \\ di_{cp_2}/dt \\ \vdots \\ di_{cp_n}/dt \end{bmatrix}}_{\mathbf{I_{cp}}}. \quad (1)$$

In the matrix $\mathbf{L}$, the element L_i represents the self-inductance of the ith phase of the coupled inductor, and the element M_{ij} represents the mutual inductance of the ith and jth phases of the coupled inductor. For an MCSCI, the self-inductances of all phases are equal, and the mutual inductances between all phases are equal. For an MCACI there is no such relationship.

The modeling method proposed in this article makes certain idealistic assumptions, considering that there will be some errors in the actual situation. The details are as follows.

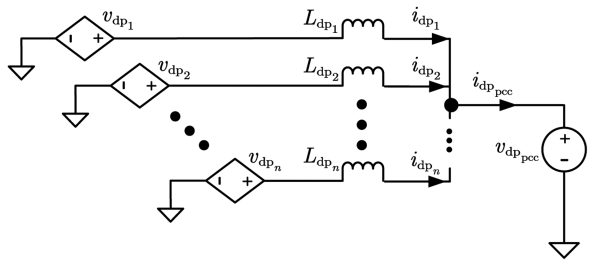

Fig. 2. Pseudodecoupled circuit of an interleaved multiphase converter with coupled inductors.

1) The performance analysis is assumed to be carried out in the continuous conduction mode (CCM) condition.
2) In deriving the formula for the peak-to-peak value of ripple, it is assumed that the inductor voltage waveforms are ideal rectangular waveforms and the inductors are ideal linear. However, due to actual input and output voltage fluctuations and the presence of parasitic parameters in the inductors, switching devices, and converter lines, the inductor voltage waveform deviates from the ideal rectangular form. Consequently, the peak-to-peak current ripple in the actual circuit will differ from the theoretical calculations presented in this article.

A. Pseudodecoupled Circuits for MCCIs

Decoupling is a common method for analyzing circuits with coupling relationships, and it requires that the current and voltage relationships remain unchanged before and after decoupling. However, it is very difficult to achieve a true decoupling of each phase for MCCIs.

In order to solve this problem, a pseudodecoupling idea is proposed in this article. The pseudodecoupling modeling method first constructs a diagonal matrix without coupling relationship based on the original inductance matrix of the multiphase coupled inductors, and then uses the proposed ripple distribution coefficient matrix to describe the coupling relationship between the phases of the inductors, which can simplify the analysis of an MCCI as an independent inductor converter. In this way, the current and voltage relationships of the circuit phases before and after pseudodecoupling are not exactly the same, but they maintain the same steady-state and transient characteristics at the point of common connection (PCC). This method helps to simplify the analysis of MCCIs and enables easier and more efficient design of controllers and inductors for MCCIs.

The pseudodecoupling operation of an MCCI is defined as follows:

$$\mathbf{L_{dp}} = \operatorname{diag}\left(\mathbf{L^{-1}p}\right)^{-1} \tag{2}$$

where $\mathbf{p}$ is an n-dimensional column vector with all elements equal to 1. The independent inductor multiphase converter with inductance matrix $\mathbf{L_{dp}}$ is defined as the pseudodecoupled equivalent circuit of the MCCI. The pseudodecoupled equivalent circuit of the MCCI is shown in Fig. 2. $L_{\mathrm{dp}i}$ is the ith element on the diagonal of the matrix $\mathbf{L_{dp}}$ and represents the ith phase pseudodecoupled inductance of the MCCI, given by

$$L_{\mathrm{dp}i} = \frac{1}{\sum_{j=1}^{n}\left(\mathbf{L}^{-1}\right)_{ij}}. \tag{3}$$

The phase voltage and phase current of the pseudodecoupled equivalent circuit are described by the inductance matrix $\mathbf{L_{dp}}$

$$\underbrace{\begin{bmatrix} v_{\mathrm{dp}_1} - v_{\mathrm{dp}_{\mathrm{pcc}}} \\ v_{\mathrm{dp}_2} - v_{\mathrm{dp}_{\mathrm{pcc}}} \\ \vdots \\ v_{\mathrm{dp}_n} - v_{\mathrm{dp}_{\mathrm{pcc}}} \end{bmatrix}}_{\mathbf{V_{dp}}} = \underbrace{\begin{bmatrix} L_{\mathrm{dp}1} & & & \\ & L_{\mathrm{dp}2} & & \\ & & \ddots & \\ & & & L_{\mathrm{dp}n} \end{bmatrix}}_{\mathbf{L_{dp}}} \underbrace{\begin{bmatrix} di_{\mathrm{dp}_1}/dt \\ di_{\mathrm{dp}_2}/dt \\ \vdots \\ di_{\mathrm{dp}_3}/dt \end{bmatrix}}_{\mathbf{I_{dp}}}. \tag{4}$$

If $\mathbf{V_{dp}} = \mathbf{V_{cp}} = \mathbf{V}$, substituting (4) into (1) yields

$$\underbrace{\begin{bmatrix} di_{\mathrm{cp}_1}/dt \\ di_{\mathrm{cp}_2}/dt \\ \vdots \\ di_{\mathrm{cp}_n}/dt \end{bmatrix}}_{\mathbf{I_{cp}}} = \underbrace{\begin{bmatrix} \delta_{11} & \delta_{12} & \cdots & \delta_{1n} \\ \delta_{21} & \delta_{22} & \cdots & \delta_{2n} \\ \vdots & \vdots & \ddots & \vdots \\ \delta_{n1} & \delta_{n2} & \cdots & \delta_{nn} \end{bmatrix}}_{\boldsymbol{\delta}} \underbrace{\begin{bmatrix} di_{\mathrm{dp}_1}/dt \\ di_{\mathrm{dp}_2}/dt \\ \vdots \\ di_{\mathrm{dp}_n}/dt \end{bmatrix}}_{\mathbf{I_{dp}}} \tag{5}$$

where $\boldsymbol{\delta} = \mathbf{L^{-1}L_{dp}} = \mathbf{L^{-1}diag(L^{-1}p)^{-1}}$ is defined as the ripple distribution coefficient matrix, with δ_{ij} in the matrix representing the ripple distribution coefficient from phase *j* to phase *i*. In particular, it should be noted that δ_{ij} and δ_{ji} are not necessarily equal due to asymmetrical coupling. The formula for calculating δ_{ij} is

$$\delta_{ij} = \frac{\left(\mathbf{L}^{-1}\right)_{ij}}{\sum_{j=1}^{n}\left(\mathbf{L}^{-1}\right)_{ij}}. \tag{6}$$

There is $\sum_{j=1}^{n}\delta_{ij} = 1$, so the phase current change rates of an MCCI can be seen as the result of redistributing and recombining the phase current change rates from its pseudodecoupled circuit. The current change rate at the PCC of both the MCCI and its pseudodecoupled circuit is the same, viz

$$di_{\mathrm{cp}_{\mathrm{pcc}}}/dt = di_{\mathrm{dp}_{\mathrm{pcc}}}/dt. \tag{7}$$

Specifically, when all elements of the voltage vector $\mathbf{V}$ are equal, where V_i represents the ith element of vector $\mathbf{V}$, and namely, when $V_1 = V_2 = \ldots = V_n = v$, it follows that:

$$\mathbf{V} = \mathbf{L_{dp}I_{cp}}. \tag{8}$$

That is, $\mathbf{I_{cp}} = \mathbf{I_{dp}}$, meaning the phase current of an MCCI varies in agreement with its pseudodecoupled circuit. The detailed proof procedure is shown in Appendix A.

B. Transient Performance Analysis

The dynamic characteristics of converters at their operating points is crucial for designing coupled inductors with optimal transient performance. The transient performance of an MCCI can be analyzed based on the switching period averaging method [29].

By applying the switching period averaging method to (1), we get

$$\underbrace{\begin{bmatrix} \hat{v}_{\mathrm{cp}_1} - \hat{v}_{cp_{\mathrm{pcc}}} \\ \hat{v}_{\mathrm{cp}_1} - \hat{v}_{cp_{\mathrm{pcc}}} \\ \vdots \\ \hat{v}_{\mathrm{cp}_1} - \hat{v}_{cp_{\mathrm{pcc}}} \end{bmatrix}}_{\hat{\mathbf{V}}_{\mathbf{cp}}} = \underbrace{\begin{bmatrix} L_1 & M_{12} & \cdots & M_{1n} \\ M_{21} & L_2 & \cdots & M_{2n} \\ \vdots & \vdots & \ddots & \vdots \\ M_{n1} & M_{n2} & \cdots & L_n \end{bmatrix}}_{\mathbf{L}} \underbrace{\begin{bmatrix} d\hat{i}_{\mathrm{cp}_1}/dt \\ d\hat{i}_{\mathrm{cp}_2}/dt \\ \vdots \\ d\hat{i}_{\mathrm{cp}_n}/dt \end{bmatrix}}_{\hat{\mathbf{I}}_{\mathbf{cp}}} \tag{9}$$

where $\hat{v}_{\mathrm{cp}_1}$ denotes the switching cycle average perturbation of variable v_{cp_1}. Similarly, switching cycle averaging is performed for the pseudodecoupled circuit as follows:

$$\hat{\mathbf{V}} = \mathbf{L_{dp}}\hat{\mathbf{I}}_{\mathbf{dp}} \tag{10}$$

when $\hat{\mathbf{V}}_{\mathbf{dp}} = \hat{\mathbf{V}}_{\mathbf{cp}} = \hat{\mathbf{V}}$. Then, using the property of the pseudodecoupled equivalent circuit, it can be said that

$$\hat{\mathbf{I}}_{\mathbf{cp}} = \boldsymbol{\delta}\hat{\mathbf{I}}_{\mathbf{dp}}, \tag{11}$$

$$d\hat{i}_{\mathrm{cp}_{\mathrm{pcc}}}/dt = d\hat{i}_{\mathrm{dp}_{\mathrm{pcc}}}/dt. \tag{12}$$

Therefore, an MCCI and its pseudodecoupled circuit are considered to have the same transient characteristics at the PCC. The transient characteristics of each phase of the MCCI can also be analyzed by (11) using the pseudodecoupled circuit.

1) Transient Performance Under Common-Mode Perturbations: In particular, when a common-mode voltage perturbation is introduced into the MCCI, i.e., when the same voltage perturbation is introduced into each phase, the following can be derived according to the characteristics of the pseudodecoupled circuit:

$$\hat{\mathbf{V}} = \mathbf{L_{dp}}\hat{\mathbf{I}}_{\mathbf{cp}}. \tag{13}$$

In MCCI, the tracking control tends to introduce the same duty cycle variation in each phase, which can be approximated as introducing a common-mode voltage perturbation to the MCCI. Therefore, the equivalent transient inductance of each phase under the common-mode voltage perturbation can be used to evaluate the transient performance of each phase of the MCCI. The smaller the equivalent common-mode transient inductance, the faster the MCCI response. Let $L_{\mathrm{tr}i}$ be the equivalent common-mode transient inductance of the ith phase of the MCCI. According to (13), we have

$$L_{\mathrm{tr}i} = L_{\mathrm{dp}i}. \tag{14}$$

Under the common-mode voltage perturbation, the current at the PCC of the MCCI is given by

$$\hat{v} = \frac{1}{\sum_{i=1}^{n}\sum_{j=1}^{n}\left(\mathbf{L}^{-1}\right)_{ij}} \frac{d\hat{i}_{\mathrm{cp}_{\mathrm{pcc}}}}{dt}. \tag{15}$$

Therefore, $L_{\mathrm{tr}_{\mathrm{pcc}}} = 1/(\mathbf{p}^T\mathbf{L}^{-1}\mathbf{p})$ is defined as the equivalent common mode transient inductance at the PCC of the MCCI, which is used to evaluate the transient performance at the PCC of the MCCI.

2) Transient Performance Under Differential-Mode Perturbations: When a differential mode voltage perturbation is introduced, the relationship between the voltage difference and current difference of each phase has to be studied [20]. Taking the example of introducing perturbation $\hat{v}$ in the first phase of an MCCI, i.e., setting $\hat{\mathbf{V}} = [\hat{v}, 0, \ldots, 0]^T$ and constructing the transformation matrix $\mathbf{T}$

$$\mathbf{T} = \begin{bmatrix} 1 & 1 & 1 & \cdots & 1 \\ 1 & -1 & 0 & \cdots & 0 \\ 1 & 0 & -1 & \cdots & 0 \\ \vdots & \vdots & \vdots & \ddots & \vdots \\ 1 & 0 & 0 & \cdots & -1 \end{bmatrix}. \tag{16}$$

The matrix $\mathbf{T}$ is invertible. Use this matrix to transform the current perturbation vector $\hat{\mathbf{I}}_{\mathbf{cp}}$. Let the transformed vector be $\mathbf{q_i}$

$$\mathbf{q_i} = \mathbf{T}\cdot\hat{\mathbf{I}}_{\mathbf{cp}} = \begin{bmatrix} d\left(\hat{i}_{\mathrm{cp}_1} + \hat{i}_{\mathrm{cp}_2} + \cdots + \hat{i}_{\mathrm{cp}_n}\right)/dt \\ d\left(\hat{i}_{\mathrm{cp}_1} - \hat{i}_{\mathrm{cp}_2}\right)/dt \\ \vdots \\ d\left(\hat{i}_{\mathrm{cp}_1} - \hat{i}_{\mathrm{cp}_n}\right)/dt \end{bmatrix}. \tag{17}$$

The first element of the vector $\mathbf{q_i}$ represents the sum of the current perturbation change rates for each phase of the MCCI, while the ith element (for $i \neq 1$) represents the difference between the current perturbation change rates of phase 1 and phase i. Similarly, the voltage perturbation vector $\hat{\mathbf{V}}$ is transformed and the transformed vector is set to be $\mathbf{q_v}$

$$\mathbf{q_v} = \mathbf{T}\cdot\hat{\mathbf{V}} = \begin{bmatrix} \hat{v}_1 + \hat{v}_2 + \cdots + \hat{v}_n - n\hat{v}_{\mathrm{pcc}} \\ \hat{v}_1 - \hat{v}_2 \\ \hat{v}_1 - \hat{v}_3 \\ \vdots \\ \hat{v}_1 - \hat{v}_n \end{bmatrix}. \tag{18}$$

Substitute (17) and (18) into (9)

$$\hat{\mathbf{q}}_{\mathbf{v}} = \mathbf{TLT}^{-1}\hat{\mathbf{q}}_{\mathbf{i}}. \tag{19}$$

When $\hat{\mathbf{V}} = [\hat{v}, 0, \ldots, 0]^T$, $\mathbf{q_v} = [\hat{v}, \hat{v}, \cdots \hat{v}]$, i.e., each element of the vector $\mathbf{q_v}$ is equal. Matrix $\mathbf{TLT^{-1}}$ is invertible. Thus it follows that:

$$\hat{\mathbf{q}}_{\mathbf{v}} = \mathrm{diag}\left(\mathbf{TL}^{-1}\mathbf{T}^{-1}\mathbf{p}\right)^{-1}\hat{\mathbf{q}}_{\mathbf{i}}. \tag{20}$$

The proof is similar to that of (8) and will not be repeated here. For details, please refer to Appendix A. Define

$\mathrm{diag}(\mathbf{T}\mathbf{L}^{-1}\mathbf{T}^{-1}\mathbf{p})^{-1}$ to be the equivalent differential mode transient inductance matrix $\mathbf{L_{dtr1}}$ of the first phase with

$$\mathbf{L_{dtr1}} = \begin{bmatrix} L_{\mathrm{tr1}} & & & & \\ & L_{\mathrm{dtr12}} & & & \\ & & L_{\mathrm{dtr13}} & & \\ & & & \ddots & \\ & & & & L_{\mathrm{dtr1}n} \end{bmatrix}. \quad (21)$$

L_{tr1} is the equivalent common mode transient inductance of phase 1. $L_{\mathrm{dtr1}i}$ is the equivalent differential mode transient inductance from phase 1 to phase i. The larger the $L_{\mathrm{dtr1}i}$, the less likely it is for a current difference to develop between phase 1 and phase i of the MCCI due to a differential mode voltage perturbation in phase 1. Thus the equivalent differential mode transient inductance can be used to evaluate the ability of MCCI to resist differential mode perturbations. The calculation formula for $L_{\mathrm{dtr1}i}$ is

$$L_{\mathrm{dtr1}i} = \frac{L_{\mathrm{tr1}}}{\delta_{11} - \delta_{i1}}. \quad (22)$$

The derivation of the differential mode transient inductance matrix for the remaining phases can be referred to the above steps.

C. Steady-State Current Ripple Analysis

The steady-state current ripple at each phase and the PCC affects the efficiency, reliability, and selection of filter capacitors for converters. To better understand the influence of coupling effects on current ripple, we derive current ripple formulations for MCCIs and define the equivalent steady-state inductance for evaluating the steady-state performance of MCCIs.

When the voltage vectors at steady state satisfy $\mathbf{V_{dp}} = \mathbf{V_{cp}} = \mathbf{V}$, in conjunction with (5), the following can be derived:

$$\underbrace{\begin{bmatrix} \Delta i_{\mathrm{cp}_1} \\ \Delta i_{\mathrm{cp}_2} \\ \vdots \\ \Delta i_{\mathrm{cp}_n} \end{bmatrix}}_{\Delta \mathbf{i_{cp}}} = \underbrace{\begin{bmatrix} \delta_1 & \delta_{12} & \cdots & \delta_{1n} \\ \delta_{21} & \delta_2 & \cdots & \delta_{2n} \\ \vdots & \vdots & \ddots & \vdots \\ \delta_{n1} & \delta_{n2} & \cdots & \delta_{nn} \end{bmatrix}}_{\boldsymbol{\delta}} \underbrace{\begin{bmatrix} \Delta i_{\mathrm{dp}_1} \\ \Delta i_{\mathrm{dp}_2} \\ \vdots \\ \Delta i_{\mathrm{dp}_n} \end{bmatrix}}_{\Delta \mathbf{i_{dp}}}. \quad (23)$$

The vectors $\Delta\mathbf{i_{cp}}$ and $\Delta\mathbf{i_{dp}}$, respectively, represent the phase current ripple of an MCCI and its pseudodecoupled equivalent circuit. As shown in Fig. 3, the current ripples of the phases of an MCCI can be regarded as the result of the redistribution and recombination of the current ripples of the phases of its corresponding pseudodecoupled circuits. Moreover, the current ripple Δi_{pcc} at the PCC of an MCCI is identical to that at the PCC of its pseudodecoupled equivalent circuit, being the sum of the phase current ripples of the pseudodecoupled equivalent circuit.

1) Current Ripple of Each Phase of an MCCI: Assuming that the phase inductor voltage waveforms of the MCCI and its pseudodecoupled equivalent circuit are ideal rectangular waveforms. Let the duty cycle of the inductor voltage V_i for the ith phase be D_i, the high level value be V_h, the low level value be V_l, and the switching period be $T_{\mathrm{sw}} = 1/f_{\mathrm{sw}}$. Then, the phase inductor

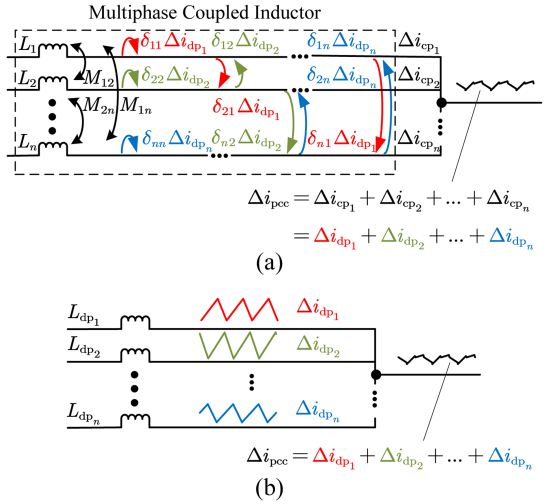

Fig. 3. Comparison of current ripple of multiphase converters. (a) Current ripple of a multiphase converter with coupled inductor. (b) Current ripple of a multiphase converter with pseudodecoupled inductor.

current ripples of the pseudodecoupled equivalent circuit are ideal triangular waveforms, and the current ripple $\Delta i_{\mathrm{dp}_i}(t)$ of the ith phase is given by

$$\Delta i_{\mathrm{dp}_i}(t) = \Delta i_{\mathrm{dp}_i}^{\mathrm{pp}} f_i(t) \quad (24)$$

where

$$f_i(t) = \begin{cases} \frac{(t-kT_{\mathrm{sw}})}{D_i T_{\mathrm{sw}}} - \frac{1}{2}, & kT \le t < (D_i + k)T \\ \frac{(T_{\mathrm{sw}} - (t-kT_{\mathrm{sw}}))}{(T_{\mathrm{sw}} - D_i T_{\mathrm{sw}})} - \frac{1}{2}, & (D_i + k)T \le t < (k+1)T \end{cases}, \quad k \in Z. \quad (25)$$

The peak-to-peak value $\Delta i_{\mathrm{dp}_i}^{\mathrm{pp}}$ can be computed as

$$\Delta i_{\mathrm{dp}_i}^{\mathrm{pp}} = \frac{D_i V_h}{L_{\mathrm{dp}_i} f_{\mathrm{sw}}} = \frac{(1 - D_i) V_l}{L_{\mathrm{dp}_i} f_{\mathrm{sw}}}. \quad (26)$$

From (23), the phase current ripple of the MCCI can be perceived as the summation of n triangular waveforms with different phase shifts. If the phase shifts of these waveforms are denoted as $\varphi_1, \varphi_2 \ldots \varphi_n$ the expression for the ith phase current ripple of the multiphase converter with coupled inductors is

$$\Delta i_{\mathrm{cp}_i}(t) = \frac{V_h}{f_{\mathrm{sw}}} \sum_{j=1}^{n} \frac{D_j \delta_{ij}}{L_{\mathrm{dp}_j}} f_j \left(t - \frac{\varphi_j}{2\pi} T_{\mathrm{sw}} \right). \quad (27)$$

For the peak-to-peak value $\Delta i_{\mathrm{cp}_i}^{\mathrm{pp}}$ of the phase current ripple of the MCCI, it can be precisely calculated using the geometric features of the triangular wave. Specifically, the sum wave $\Delta i_{\mathrm{cp}_i}(t)$ of n triangular waves has $2n$ turning points of slope which occur at the timing of the extreme points of the triangular waves. Hence, by comparing the values of all the turning points of the wave $\Delta i_{\mathrm{cp}_i}(t)$, we can obtain its maximum and minimum values, yielding the peak-to-peak value $\Delta i_{\mathrm{cp}_i}^{\mathrm{pp}}$ as

$$\Delta i_{\mathrm{cp}_i}^{\mathrm{pp}} = \max_{k=1}^{n} \left\{ \Delta i_{\mathrm{cp}_i} \left(\frac{\varphi_k}{2\pi} T_{\mathrm{sw}} \right), \Delta i_{\mathrm{cp}_i} \left(\frac{\varphi_k}{2\pi} T_{\mathrm{sw}} + D_k T_{\mathrm{sw}} \right) \right\}$$

$$-\min_{k=1}^{n}\left\{\Delta i_{\mathrm{cp}_i}\left(\frac{\varphi_k}{2\pi}T_{\mathrm{sw}}\right),\Delta i_{\mathrm{cp}_i}\left(\frac{\varphi_k}{2\pi}T_{\mathrm{sw}}+D_kT_{\mathrm{sw}}\right)\right\}. \tag{28}$$

The equivalent steady-state inductance of phase i of the MCCI can be defined as follows, which is used to evaluate the steady-state current ripple performance of phase i of the MCCI

$$L_{\mathrm{ss}_i}=\frac{D_iV_h}{f_{\mathrm{sw}}\Delta i_{\mathrm{cp}_i}^{\mathrm{pp}}}=\frac{\Delta i_{\mathrm{dp}_i}^{\mathrm{pp}}}{\Delta i_{\mathrm{cp}_i}^{\mathrm{pp}}}L_{\mathrm{dp}_i}. \tag{29}$$

In particular, based on the properties of the pseudodecoupled circuit, it is known that when the same (same phase-shift, same duty cycle, same amplitude) rectangular waveform voltage is applied to each phase of an MCCI, the equivalent steady-state inductance of each phase of the MCCI is equal to the pseudodecoupled inductance.

As a smaller L_{tr_i} indicates a faster response and a larger L_{ss_i} indicates a smaller current ripple, Ltr_i/Lss_i can be defined as the performance improvement coefficient μ_i of phase i of an MCCI, which is to evaluate the degree of performance improvement of an MCCI compared to a multiphase converter with independent inductors

$$\mu_i=\frac{L_{\mathrm{tr}_i}}{L_{\mathrm{ss}_i}}=\frac{L_{\mathrm{dp}_i}}{L_{\mathrm{ss}_i}}=\frac{\Delta i_{\mathrm{cp}_i}^{\mathrm{pp}}}{\Delta i_{\mathrm{dp}_i}^{\mathrm{pp}}}. \tag{30}$$

From (28), μ_i is a function of the duty ratio D, phase number n, and the inductance matrix $\mathbf{L}$. This indicates that, under the same operating conditions and transient characteristics, the peak-to-peak value of the current ripple of phase *i* of the MCCI is μ_i times that of the multiphase converter with independent inductors. Alternatively, if the current ripple performance is the same, the inductor current change rate of phase *i* of the multiphase converter with independent inductors under the same inductor voltage perturbation is μ_i times that of the MCCI. A smaller μ_i indicates a higher degree of improvement.

2) Current Ripple At the PCC of an MCCI: For the current ripple $\Delta i_{\mathrm{pcc}}(t)$ at the PCC, it can be calculated by the following formula:

$$\Delta i_{\mathrm{pcc}}(t)=\frac{V_h}{f_{\mathrm{sw}}}\sum_{j=1}^{n}\frac{D_j}{L_{\mathrm{dp}_j}}f_j\left(t-\frac{\varphi_j}{2\pi}T_{\mathrm{sw}}\right). \tag{31}$$

The peak-to-peak expression is

$$\begin{aligned}\Delta i_{\mathrm{pcc}}^{\mathrm{pp}}=&\max_{k=1}^{n}\left\{\Delta i_{\mathrm{pcc}}\left(\frac{\varphi_k}{2\pi}T_{\mathrm{sw}}\right),\Delta i_{\mathrm{pcc}}\left(\frac{\varphi_k}{2\pi}T_{\mathrm{sw}}+DT_{\mathrm{sw}}\right)\right\}\\&-\min_{k=1}^{n}\left\{\Delta i_{\mathrm{pcc}}\left(\frac{\varphi_k}{2\pi}T_{\mathrm{sw}}\right),\Delta i_{\mathrm{pcc}}\left(\frac{\varphi_k}{2\pi}T_{\mathrm{sw}}+DT_{\mathrm{sw}}\right)\right\}.\end{aligned} \tag{32}$$

Similarly, an equivalent steady-state inductance $L_{\mathrm{ss}_{\mathrm{pcc}}}$ at the PCC of the MCCI is defined, which is used to evaluate the steady-state performance at the PCC of the MCCI

$$L_{\mathrm{ss}_{\mathrm{pcc}}}=\frac{\bar{D}V_h}{\Delta i_{\mathrm{pcc}}^{\mathrm{pp}}f_{\mathrm{sw}}} \tag{33}$$

where $\bar{D}$ is the average value of the duty cycle of each phase.

The modeling method can also be used to evaluate the performance improvement of an MCCI compared to a single-phase converter. The performance improvement of PCC of an MCCI can be quantified as follows:

$$\mu_{\mathrm{pcc}}=\frac{L_{\mathrm{tr}_{\mathrm{pcc}}}}{L_{\mathrm{ss}_{\mathrm{pcc}}}}=\frac{\Delta i_{\mathrm{pcc}}^{\mathrm{pp}}}{\sum_{i=1}^{n}\Delta i_{\mathrm{dp}_i}^{\mathrm{pp}}}. \tag{34}$$

This indicates that, under the same operating conditions and transient characteristics, the peak-to-peak value of the current ripple at the PCC of the multiphase converter is μ_{pcc} times the peak-to-peak value of the inductor current ripple in the single-phase converter. Alternatively, if the current ripple performance is the same, the inductor current change rate in the single-phase converter under the same inductor voltage perturbation is μ_{pcc} times the inductor current change rate at the PCC of the multiphase converter.

D. Discussion of the Modeling Method

The traditional MCCI modeling method [17], [18], [19] involves multiple segmented calculations when solving for current expressions and equivalent inductance, making the entire analysis process cumbersome and time consuming, especially when dealing with a large number of phases or numerous inductance parameters, which increases the computational burden. In addition, this method requires strict conditions for analysis, such as limiting the duty cycle, phase shift, phase sequence, and topology. While these conditions help simplify the problem, they also reduce the flexibility of the model, making it unable to adapt to complex or changing working condition power electronic systems, thus limiting its applicability.

The proposed pseudodecoupling modeling method introduces the concepts of pseudodecoupling inductance and exchange coefficient, and presents general matrix expressions for equivalent transient inductance and equivalent steady-state inductance in continuous mode, significantly reducing the complexity of the solution process. Compared to the traditional modeling method, which relies on strict system configurations, the proposed method offers greater flexibility and can adapt to a wider range of MCCI topologies and operating conditions. The process of the proposed method is summarized as follows.

1) Determine the inductance matrix of coupled inductors.
2) *Pseudodecoupling of the coupled inductance:* Use (2) and (6) to calculate the pseudodecoupling inductance matrix and the exchange coefficient matrix, respectively.
3) *Transient characteristic analysis:* Use (14) to calculate the common-mode transient inductance; use (22) to calculate the differential-mode transient inductance.
4) *Steady-state characteristic analysis:* Use (28) or (32) to calculate the peak-to-peak ripple of phase currents or the peak-to-peak ripple at the PCC; Use (29) or (33) to calculate the equivalent steady-state inductance of each phase or at the PCC.

When the inductance matrix is difficult to determine, identical rectangular-waveform voltages can be applied to each phase of the MCCI. The coupled inductor's pseudodecoupled inductance can then be directly calculated from the resulting current waveforms, simplifying the analysis process.

III. Effect of Asymmetry Degree on the Performance of Multiphase Converters With Coupled Inductors

A. Performance Analysis of Multiphase Converters With Symmetrical Coupled Inductors

To quantitatively discuss the effect of asymmetrical parameters on the performance of an MCCI, an MCSCI is first analyzed. Let the symmetrical multiphase coupled inductor self-inductance of each phase be L, the mutual inductance of each phase be M, the coupling coefficient be $\alpha = \frac{(n-1)M}{L}$, and its inductance matrix $\mathbf{L}_{\rm sym}$ be

$$\mathbf{L}_{\rm sym} = \begin{bmatrix} L & M & \cdots & M \\ M & L & \cdots & M \\ \vdots & \vdots & \ddots & \vdots \\ M & M & \cdots & L \end{bmatrix}. \tag{35}$$

1) Pseudodecoupling of an MCSCI: Substituting (35) into (3), it can be seen that the pseudodecoupled inductance of each phase of MCSCI is equal, and the pseudodecoupled inductance of MCSCI can be calculated as follows:

$$L_{\rm dp}^{\rm sym} = L + (n-1)\,M = (1+\alpha)\,L. \tag{36}$$

Substituting (35) into (6), the ripple distribution coefficient matrix $\boldsymbol{\delta}_{\rm sym}$ of MCSCI is

$$\boldsymbol{\delta}_{\rm sym} = \begin{bmatrix} \delta_s & \delta & \cdots & \delta \\ \delta & \delta_s & \cdots & \delta \\ \vdots & \vdots & \ddots & \vdots \\ \delta & \delta & \cdots & \delta_s \end{bmatrix} \tag{37}$$

where

$$\delta = \frac{-M}{L-M} = \frac{-\alpha}{n-1-\alpha}, \tag{38}$$

$$\delta_s = \frac{L+(n-2)\,M}{L-M} = \frac{n-1+(n-2)\alpha}{n-1-\alpha}. \tag{39}$$

2) Transient Performance Analysis of an MCSCI: According to the analysis in Section II, the equivalent common-mode transient inductance of each phase of the MCCI is equal to the pseudodecoupled inductance. Therefore, the equivalent common-mode transient inductance of each phase of the MCSCI is the same and is denoted as $L_{\rm tr}^{\rm sym}$. Thus, we have

$$L_{\rm tr}^{\rm sym} = L_{\rm dp}^{\rm sym} = L + (n-1)\,M = (1+\alpha)\,L. \tag{40}$$

The equivalent common-mode transient inductance at the PCC of MCSCI is set to be $L_{{\rm tr}_{\rm pcc}}^{\rm sym}$, with

$$L_{{\rm tr}_{\rm pcc}}^{\rm sym} = \frac{L+(n-1)\,M}{n} = \frac{(1+\alpha)}{n}L. \tag{41}$$

By substituting (36) and (37) into (6), it is evident that the equivalent differential mode transient inductance between the phases of the MCSCI is equal, denoted as $L_{\rm dtr}^{\rm sym}$, and is given by

$$L_{\rm dtr}^{\rm sym} = \frac{L_{\rm tr}^{\rm sym}}{\delta_s - \delta} = L - M = \left(1 - \frac{\alpha}{n-1}\right)L. \tag{42}$$

From the above analysis, it can be seen that the inverse coupling ($\alpha < 0$) of the coupled inductors enables the MCSCI to have a smaller common-mode transient inductance and a larger differential-mode transient inductance. This means that an inversely coupled MCSCI can respond faster to load variations and is less prone to phase-to-phase current differences due to differential-mode voltage perturbations, thus exhibiting more desirable transient performance.

3) Steady-State Performance Analysis of an MCSCI: Because the coupled inductors are symmetrical, setting the duty cycle of each phase as D and the phase shift of each phase differs by $2\pi/n$ in turn. Substituting (36) into (12), the pseudodecoupled circuit of an MCSCI has equal current ripple peak-to-peak value $\Delta i_{\rm dp}^{\rm pp}$ for each phase, with

$$\Delta i_{\rm dp}^{\rm pp} = \frac{DV_h}{f_{\rm sw}\left[L+(n-1)\,M\right]}. \tag{43}$$

The current ripple at the PCC of an MCSCI can be viewed as the summation of n triangular waves, all with identical shapes but each shifted by $2\pi/n$. The formula to calculate the current ripple peak-to-peak value $\Delta i_{\rm pcc}^{\rm pp}$ at the PCC of an MCSCI can be written as

$$\Delta i_{\rm pcc}^{\rm pp} = n\Delta i_{\rm dp}^{\rm pp}\cdot F_c = \frac{nDV_h}{f_{\rm sw}\left[L+(n-1)\,M\right]}\cdot F_c \tag{44}$$

where F_c is defined as the cancellation factor, which is equal to $\mu_{\rm pcc}$ under symmetric conditions, given by

$$F_c = \frac{(k+1-Dn)\,(Dn-k)}{(1-D)\,Dn^2} \tag{45}$$

where k is the index for the duty ratio D range, and it is given by $\frac{k}{n} \le D < \frac{k+1}{n}$. When $D = \frac{k}{n}$, $F_c = 0$, and if the number of converter phases is odd, i.e., $n = 2i+1$, then when $D = 0.5$, $F_c = 1/(2i+1)^2$. Since $\mu_{\rm pcc} = F_c$ in the symmetric case, it can be concluded that the more phases there are, the better the performance of the converter. However, the performance improvement becomes smaller as the number of phases increases.

Therefore, the current ripple of each phase can be perceived as the summation of n triangular waves, where only one has a different peak-to-peak value, and the others have identical shapes but each shifted by $2\pi/n$. Using (44), the ripple expression can be simplified as follows:

$$\Delta i_{\rm cp}^{\rm pp} = n\delta\Delta i_{\rm dp}^{\rm pp}\cdot F_c + (\delta_s - \delta)\,\Delta i_{\rm dp}^{\rm pp}. \tag{46}$$

Correspondingly, the performance improvement coefficient μ_s of each phase of an MCSCI can be calculated as follows:

$$\mu_s = \frac{\Delta i_{\rm cp}^{\rm pp}}{\Delta i_{\rm dp}^{\rm pp}} = n\delta\cdot F_c + (\delta_s - \delta) = \frac{L - M + nM\,(1-F_c)}{L-M}. \tag{47}$$

Rewrite the above equation in terms of the coupling coefficient α

$$\mu_s = \frac{n-1-\alpha+n\alpha\,(1-F_c)}{n-1-\alpha}. \tag{48}$$

Fig. 4 is a graphical interpretation of the phase current ripple analysis. Expression (46) can be obtained quite intuitively by equating Fig. 4(a) to (b). It can be clearly observed that in the case of symmetry, the phase current ripple period of the

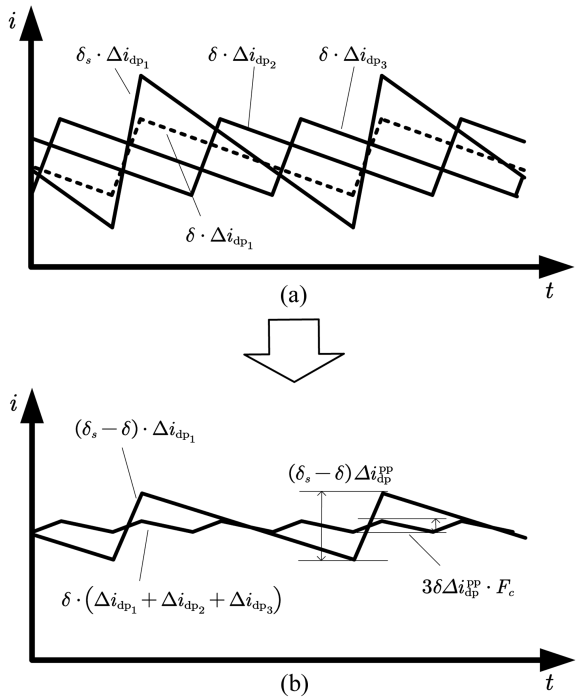

Fig. 4. Graphical interpretation of phase current ripple analysis of symmetrical coupled inductors (Taking a three-phase inductor as an example, assuming $\delta_s = \delta_{11}$, $\delta = \delta_{12} = \delta_{13}$, $\Delta i_{dp}^{pp} = \Delta i_{dp_1}^{pp} = \Delta i_{dp_2}^{pp} = \Delta i_{dp_3}^{pp}$.) (a) Phase current ripple Δi_{cp_1} can be viewed as the sum of triangular waves $\delta_s \Delta i_{dp1}$, $\delta \Delta i_{dp2}$, and $\delta \Delta i_{dp3}$. (b) Phase current ripple Δi_{cp_1} can be viewed as the sum of triangular waves $(\delta_s - \delta)\Delta i_{dp}$ and $\delta(\Delta i_{dp1} + \Delta i_{dp2} + \Delta i_{dp3})$.

multiphase converter with coupled inductor remains unchanged at T. According to (48), if n and F_c are regarded as constants, then μ_s can be regarded as a fractional linear function of the coupling coefficient α. Based on the properties of fractional linear functions, μ_s is monotonically increasing within its domain of definition. Specifically, $\mu_s = F_c$ when $\alpha = -1$, and $\mu_s = 1$ when $\alpha = 0$. Therefore, it is not possible for μ_s to be less than the cancellation factor F_c. the tighter the inverse coupling ($\alpha < 0$ and α has a larger absolute value), the better the performance of the MCSCI. Conversely, the tighter the positive coupling ($\alpha > 0$ and α has a larger absolute value), the worse the performance of the MCSCI. These insights from the analysis of the coupled inductor in symmetrical situations are equivalent to the results of previous literature studies [17], [18], [20], [21].

B. Effect of Self-Inductance Deviation

As an example, the deviation Dev_1 present in the self-inductance of the first phase of the MCCI is discussed. In this case, the inductance matrix $\mathbf{L}_{Dev1}$ of the coupled inductor is set to be

$$\mathbf{L}_{Dev1} = \begin{bmatrix} L(1+Dev_1) & M & \cdots & M \\ M & L & \cdots & M \\ \vdots & \vdots & \ddots & \vdots \\ M & M & \cdots & L \end{bmatrix} \tag{49}$$

where $|(n-1)M| < L(1+Dev_1)$, i.e., the coupling coefficient α satisfies $|\alpha| < 1 + Dev_1$.

1) Effect of Self-Inductance Deviation on Pseudodecoupling Parameters: The analysis in Section II shows that the pseudodecoupled parameters of an MCCI directly determines the transient and steady-state performance of the converter. Therefore it is important to understand the effect of self-inductance deviation on the pseudodecoupled inductances and ripple distribution coefficients. Substituting (49) into (2), the pseudodecoupled inductance matrix $\mathbf{L}_{\mathbf{dp}}^{Dev1}$ with the self-inductance deviation Dev_1 is given by

$$\mathbf{L}_{\mathbf{dp}}^{Dev1} = \begin{bmatrix} L_{\mathrm{dp1}}^{Dev1} & & & \\ & L_{\mathrm{dp}}^{Dev1} & & \\ & & \ddots & \\ & & & L_{\mathrm{dp}}^{Dev1} \end{bmatrix} \tag{50}$$

where

$$L_{\mathrm{dp1}}^{Dev1} = \frac{(L+(n-1)M)(L-M+L\cdot Dev_1) - LM\cdot Dev_1}{(L-M)}, \tag{51}$$

$$L_{\mathrm{dp}}^{Dev1} = \frac{(L+(n-1)M)(L-M+L\cdot Dev_1) - LM\cdot Dev_1}{(L-M+L\cdot Dev_1)}. \tag{52}$$

The self-inductance deviation Dev_1 makes the pseudodecoupled inductance of phase 1 different from that of the remaining phases. The pseudodecoupled inductance deviation Dev_{dp1} due to the self-inductance deviation Dev_1 can be calculated as follows:

$$Dev_{\mathrm{dp1}} = \frac{L_{\mathrm{dp1}}^{Dev1} - L_{\mathrm{dp}}^{Dev1}}{L_{\mathrm{dp}}^{Dev1}} = \frac{L\cdot Dev_1}{L-M}. \tag{53}$$

Rewrite the above equation in terms of the coupling coefficient α

$$Dev_{\mathrm{dp1}} = \frac{Dev_1}{1-\alpha/(n-1)}. \tag{54}$$

Fig. 5(a) shows the curves of the pseudodecoupled inductance deviation Dev_{dp1} according to (54) when the self-inductance deviation $Dev_1 = 0.5$. It can be found that the inverse coupling (i.e., coupling coefficient $\alpha < 0$) can reduce the impact of self-inductance deviation Dev_1. The tighter the inverse coupling (the larger the absolute value of the coupling coefficient α), the smaller the pseudodecoupled inductance deviation Dev_{dp1}. Moreover, as the phase number n increases, the pseudodecoupled inductance deviation Dev_{dp1} increases.

Substituting (49) into (6), the ripple distribution coefficient matrix $\boldsymbol{\delta}_{Dev1}$ with the self-inductance deviation is given by

$$\boldsymbol{\delta}_{Dev1} = \begin{bmatrix} \delta_s & \delta_1 & \cdots & \delta_1 \\ \delta & \delta_2 & \cdots & \delta \\ \vdots & \vdots & \ddots & \vdots \\ \delta & \delta & \cdots & \delta_2 \end{bmatrix}. \tag{55}$$

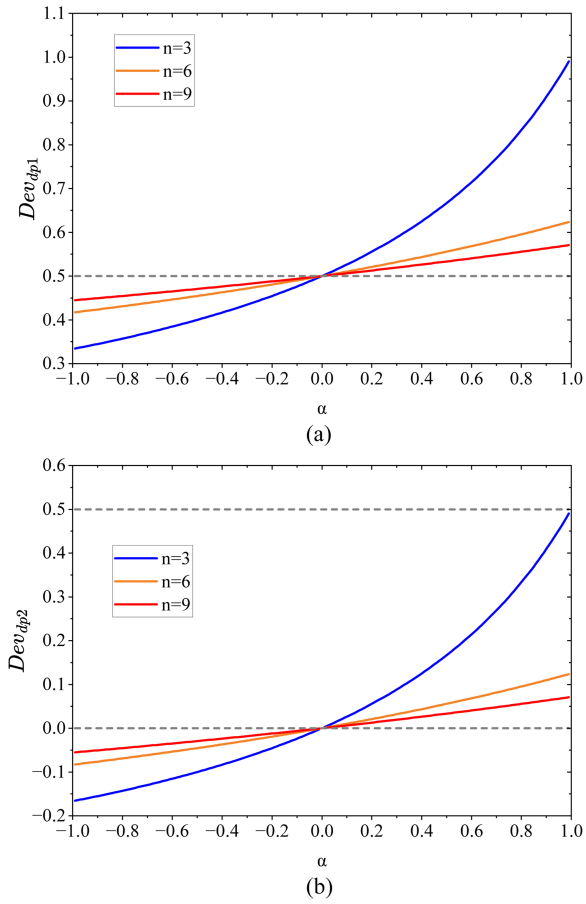

Fig. 5. Effect on the pseudodecoupled inductance deviation to each phase. (a) Effect of phase 1 self-inductance deviation ($Dev_1 = 0.5$). (b) Effect of mutual inductance deviation ($Dev_2 = 0.5$).

It can be noticed that the ripple distribution coefficient δ_1 and δ_2 are different from that in the symmetrical condition, where

$$\delta_1 = -\frac{M}{L - M + L \cdot Dev_1}, \tag{56}$$

$$\delta_2 = \frac{[(Dev_1 + 1)L - M][L + (n-2)M] - LM \cdot Dev_1}{(L - M)((1 + Dev_1)L - M)}. \tag{57}$$

2) Effect of Self-Inductance Deviation on Transient Performances: The equivalent common-mode transient inductance of each phase of the MCCI is equal to the pseudodecoupled inductance. Therefore, the common-mode transient inductance of each phase of the MCCI with self-inductance deviation can also be calculated by (51) and (52).

The variation in pseudodecoupled inductance (also the common-mode transient inductance) of phase 1 due to self-inductance deviation Dev_1, relative to the symmetrical condition, can be calculated by (58). The variation in pseudodecoupled inductances (also the common-mode transient inductances) of the remaining phases relative to the symmetrical condition can be calculated by (59). The variation in common-mode transient inductance of the PCC relative to the symmetrical condition can

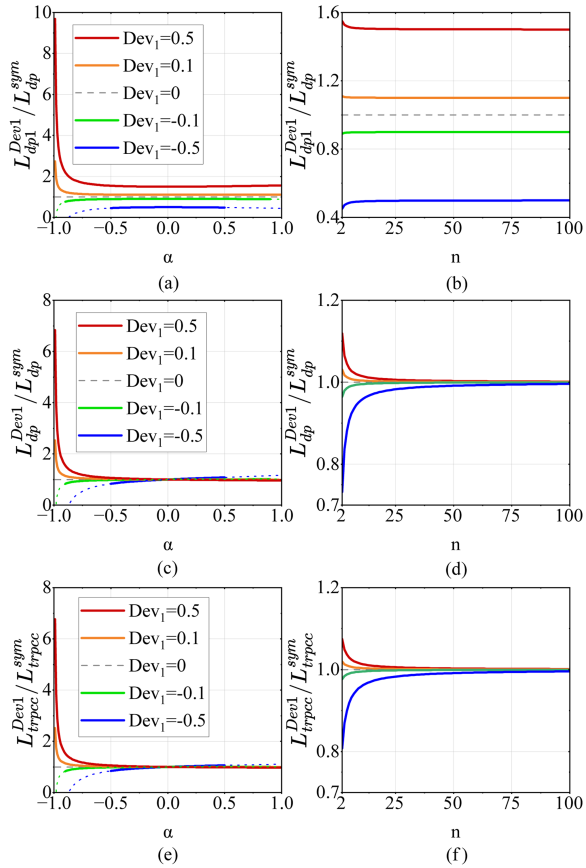

Fig. 6. Effect of the self-inductance deviation Dev_1 on each pseudodecoupled inductance parameter. (a) Effect of Dev_1 and α on $L_{\mathrm{dp1}}^{Dev1}/L_{\mathrm{dp}}^{\mathrm{sym}}$ when $n = 6$. (b) Effect of Dev_1 and n on $L_{\mathrm{dp1}}^{Dev1}/L_{\mathrm{dp}}^{\mathrm{sym}}$ when $\alpha = -0.3$. (c) Effect of Dev_1 and α on $L_{\mathrm{dp}}^{Dev1}/L_{\mathrm{dp}}^{\mathrm{sym}}$ when $n = 6$. (d) Effect of Dev_1 and n on $L_{\mathrm{dp}}^{Dev1}/L_{\mathrm{dp}}^{\mathrm{sym}}$ when $\alpha = -0.3$. (e) Effect of Dev_1 and α on $L_{\mathrm{tr_{pcc}}}^{Dev1}/L_{\mathrm{dp}}^{\mathrm{sym}}$ when $n = 6$. (f) Effect of Dev_1 and n on $L_{\mathrm{tr_{pcc}}}^{Dev1}/L_{\mathrm{dp}}^{\mathrm{sym}}$ when $\alpha = -0.3$.

be calculated by (60).

$$L_{\mathrm{dp1}}^{Dev1}/L_{\mathrm{dp}}^{\mathrm{sym}} = \frac{(1+\alpha)(1-\alpha/(n-1)+Dev_1) - \alpha \cdot Dev_1/(n-1)}{(1-\alpha/(n-1))(1+\alpha)} \tag{58}$$

$$L_{\mathrm{dp}}^{Dev1}/L_{\mathrm{dp}}^{\mathrm{sym}} = \frac{(1+\alpha)(1-\alpha/(n-1)+Dev_1) - \alpha \cdot Dev_1/(n-1)}{(1+\alpha)(1-\alpha/(n-1)+Dev_1)} \tag{59}$$

$$L_{\mathrm{tr_{pcc}}}^{Dev1}/L_{\mathrm{tr_{pcc}}}^{\mathrm{sym}} = \frac{n[(1+\alpha)(1-\alpha/(n-1)+Dev_1) - \alpha \cdot Dev_1/(n-1)]}{(1+\alpha)[n(1-\alpha/(n-1)+Dev_1) - \alpha \cdot Dev_1/(n-1)]}. \tag{60}$$

Fig. 6, based on (58), (59), and (60), illustrates the effect of the self-inductance deviation Dev_1 on pseudodecoupled inductance parameters. It can be observed that the pseudodecoupled inductance of phase 1 is most affected by self-inductance deviation

Dev_1. In the case of inverse coupling, a positive self-inductance deviation Dev_1 increases the pseudodecoupled inductance of each phase and the equivalent transient inductance at the PCC. As the self-inductance deviation increases, the increase in the pseudodecoupled inductance of the phases and the equivalent transient inductance at the PCC also increases. The greater the number of phases n, the smaller the effect of the self-inductance deviation, but this effect becomes less pronounced if n 20. In the case of inverse coupling, the tighter the coupling, the greater the effect of the deviation, and this effect becomes significant after the coupling coefficient α reaches -0.8.

For the equivalent differential mode transient inductance, combining (6), (50), and (55), it can be seen that the self-inductance deviation causes the differential mode transient inductance L_{dtr1}^{Dev1} from phase 1 to the remaining phases to be unequal to the differential mode transient inductance L_{dtr}^{Dev1} between the remaining phases, as shown in

$$L_{\mathrm{dtr1}}^{Dev1} = \frac{L_{\mathrm{dp1}}^{Dev1}}{\delta_s - \delta}. \tag{61}$$

$$L_{\mathrm{dtr}}^{Dev1} = \frac{L_{\mathrm{dp}}^{Dev1}}{\delta_2 - \delta}. \tag{62}$$

3) Effect of Self-Inductance Deviation on Steady-State Performances: Substituting (50) and (55) into (27), the peak-to-peak value of current ripples $\Delta i_{\mathrm{cp1}(Dev1)}^{\mathrm{pp}}$ of phase 1 of the MCCI with the self-inductance deviation Dev_1 can be calculated as follows:

$$\Delta i_{\mathrm{cp1}(Dev1)}^{\mathrm{pp}} = \frac{L_{\mathrm{dp}}^{\mathrm{sym}}}{L_{\mathrm{dp}}^{Dev1}} \Delta i_{\mathrm{dp}}^{\mathrm{pp}} \left[n\delta_1 \cdot F_c + \left(\delta_s \frac{Dev_1}{\sigma Dev_{\mathrm{dp1}}} - \delta_1 \right) \right]. \tag{63}$$

A comparison of (63) and (46) shows that with the self-inductance deviation Dev_1, the composition of the current ripple in phase 1 of the MCCI is similar to that in the MCSCI, except that each component is multiplied by a different factor.

Similarly, the peak-to-peak value of current ripple $\Delta i_{\mathrm{cp}i(Dev1)}^{\mathrm{pp}}$ of the phase i (for $i \neq 1$) is calculated as follows:

$$\Delta i_{\mathrm{cp}i(Dev1)}^{\mathrm{pp}} = \frac{L_{\mathrm{dp}}^{\mathrm{sym}}}{L_{\mathrm{dp}}^{Dev1}} \Delta i_{\mathrm{dp}}^{\mathrm{pp}} \left[n\delta \cdot F_c + (\delta_2 - \delta) + \gamma_{1i} \cdot \delta \frac{-Dev_{\mathrm{dp1}}}{1 + Dev_{\mathrm{dp1}}} \right] \tag{64}$$

where the coefficient γ_{1i} depends on the phase difference between the PWM of phase 1 and phase i. Fig. 8 shows the current ripple of phase 4 of a four-phase MCCI with each phase PWM shifted by $2\pi/n$ in turn as an example of the phase current ripple. Compared to the phase current ripples in the MCSCI, the phase 1 self-inductance deviation adds a triangular waveform component to the current ripples in other phases of the MCCI. The additional triangular waveform component makes it possible for the location of the peak point to change and not necessarily be at the original peak point in this phase. And the phase ripple peak value may increase or decrease relative to the symmetry, when the PWM phase difference is within $\pi/2$, as shown in Fig. 8(a), then the ripple peak value may increase relative to the symmetry; when the PWM phase difference is more than $\pi/2$, as shown in Fig. 8(b), then the ripple peak value may decrease.

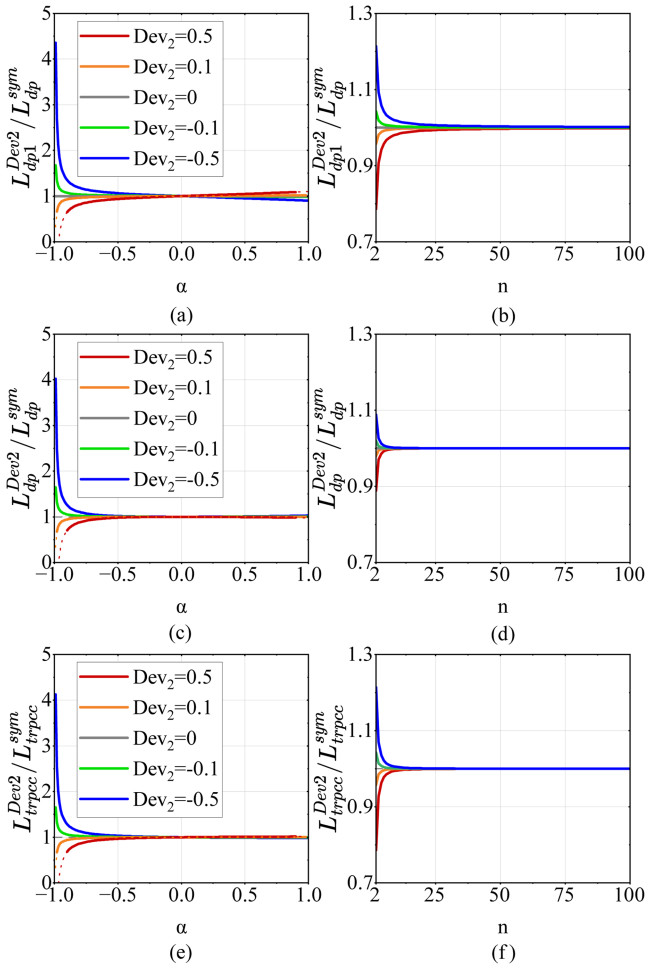

Fig. 7. Effect of the mutual inductance deviation Dev_2 on each pseudodecoupled inductance parameter. (a) Effect of Dev_2 and α on $L_{\mathrm{dp1}}^{Dev2}/L_{\mathrm{dp}}^{\mathrm{sym}}$ when $n = 6$. (b) Effect of Dev_2 and n on $L_{\mathrm{dp1}}^{Dev2}/L_{\mathrm{dp}}^{\mathrm{sym}}$ when $\alpha = -0.3$. (c) Effect of Dev_2 and α on $L_{\mathrm{dp}}^{Dev2}/L_{\mathrm{dp}}^{\mathrm{sym}}$ when $n = 6$. (d) Effect of Dev_2 and n on $L_{\mathrm{dp}}^{Dev2}/L_{\mathrm{dp}}^{\mathrm{sym}}$ when $\alpha = -0.3$. (e) Effect of Dev_2 and α on $L_{\mathrm{tr_{pcc}}}^{Dev2}/L_{\mathrm{dp}}^{\mathrm{sym}}$ when $n = 6$. (f) Effect of Dev_2 and n on $L_{\mathrm{tr_{pcc}}}^{Dev2}/L_{\mathrm{dp}}^{\mathrm{sym}}$ when $\alpha = -0.3$.

The peak-to-peak value of current ripple $\Delta i_{\mathrm{pcc}(Dev1)}^{\mathrm{pp}}$ at the PCC can be calculated by the following equation:

$$\Delta i_{\mathrm{pcc}(Dev1)}^{\mathrm{pp}} = n\Delta i_{\mathrm{dp}}^{\mathrm{pp}} \cdot \left(F_c - \frac{Dev_{\mathrm{dp1}}}{n\,(1 + Dev_{\mathrm{dp1}})} \right). \tag{65}$$

The current ripple at the PCC of the MCCI with the self-inductance deviation Dev_1 is similar to the phase current ripple of MCSCI shown in Fig. 4. Considering the characteristics of the inverse proportional function, it can be seen that if the deviation is negative, it becomes impossible for the current ripple at the PCC to be reduced to 0, as it would be in an MCSCI. Compared to an MCSCI, a higher number of phases is required to achieve the same low current ripple.

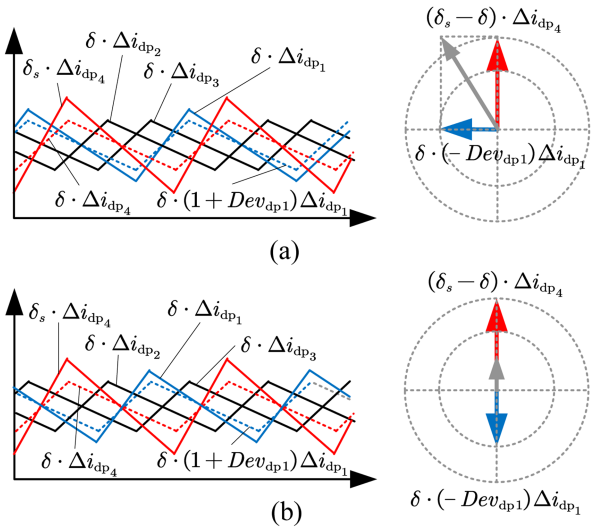

Fig. 8. Two possibilities of phase current ripple in the nonfirst phase of the MCCI with the phase 1 self-inductance deviation Dev_1 (Taking a four-phase coupled inductor as an example). (a) Asymmetry increases phase current ripple. (b) Asymmetry reduces phase current ripple.

$\mu_{\rm pcc}$ at this case

$$\mu_{\rm pcc}=\frac{F_c-\frac{Dev_{\rm dp1}}{n(1+Dev_{\rm dp1})}}{1-\frac{Dev_{\rm dp1}}{n(1+Dev_{\rm dp1})}}. \tag{66}$$

As the number of phases n increases, $\mu_{\rm pcc}$ of the MCCI with self-inductance deviation gets closer to F_c.

C. Effect of Mutual Inductance Deviation

As an example, the deviation Dev_2 present in the mutual inductance between the phase 1 and phase 2 of an MCCI is discussed. In this case, the inductance matrix $\mathbf{L}_{Dev2}$ of the coupled inductor is set to be

$$\mathbf{L}_{Dev2}=\begin{bmatrix} L & M\,(1+Dev_2) & \cdots & M \\ M\,(1+Dev_2) & L & \cdots & M \\ \vdots & \vdots & \ddots & \vdots \\ M & M & \cdots & L \end{bmatrix} \tag{67}$$

where $|(n-1+Dev_2)M|<L$, i.e., the coupling coefficient α satisfies $|\alpha|<\frac{n-1}{n-1+Dev_2}$.

1) Effect of Mutual Inductance Deviation on Pseudodecoupling Parameters: Substituting (67) into (2), the pseudodecoupled inductance matrix $\mathbf{L}_{\mathbf{dp}}^{Dev2}$ with the mutual inductance deviation is given by

$$\mathbf{L}_{\mathbf{dp}}^{Dev2}=\begin{bmatrix} L_{\rm dp1}^{Dev2} & & & \\ & L_{\rm dp2}^{Dev2} & & \\ & & \ddots & \\ & & & L_{\rm dp}^{Dev2} \end{bmatrix} \tag{68}$$

where

$$L_{\rm dp1}^{Dev2}=L_{\rm dp2}^{Dev2}=\frac{(L+(n-1)\,M)\,(L-M+M\cdot Dev_2)-2M^2\cdot Dev_2}{(L-M)}, \tag{69}$$

$$L_{\rm dp}^{Dev2}=\frac{(L+(n-1)\,M)\,(L-M+M\cdot Dev_2)-2M^2\cdot Dev_2}{(L-M+M\cdot Dev_2)}. \tag{70}$$

The mutual inductance deviation Dev_2 makes the pseudodecoupled inductance of phases 1 and 2 different from that of the remaining phases. The pseudodecoupled inductance deviation $Dev_{\rm dp2}$ due to the mutual inductance deviation Dev_2 can be calculated as follows:

$$Dev_{\rm dp2}=\frac{L_{\rm dp1}^{Dev2}-L_{\rm dp}^{Dev2}}{L_{\rm dp}^{Dev2}}=\frac{M\cdot Dev_2}{L-M}. \tag{71}$$

Rewrite the above equation in terms of the coupling coefficient α

$$Dev_{\rm dp2}=\begin{cases}\frac{Dev_2}{(n-1)/\alpha-1} & ,\alpha\neq 0\\ 0 & ,\alpha=0\end{cases}. \tag{72}$$

Fig. 5(b) shows the curve of the pseudodecoupled inductance deviation $Dev_{\rm dp2}$ according to (72) when the mutual inductance deviation $Dev_2=0.5$. It can be found that under inverse coupling (i.e., coupling coefficient $\alpha<0$), the mutual inductance deviation Dev_2 brings about the opposite pseudodecoupled inductance deviation $Dev_{\rm dp2}$. The tighter the inverse coupling (the larger the absolute value of the coupling coefficient α), the larger the absolute value of the pseudodecoupled inductance deviation. Moreover, as the phase number n increases, the absolute value of the pseudodecoupled inductance deviation $Dev_{\rm dp2}$ decreases.

Substituting (67) into (6), the ripple distribution coefficient matrix $\boldsymbol{\delta}_{Dev2}$ with the mutual inductance deviation is given by

$$\boldsymbol{\delta}_{Dev2}=\begin{bmatrix} \delta_5 & \delta_4 & \delta_3 & \cdots & \delta_3 \\ \delta_4 & \delta_5 & \delta_3 & \cdots & \delta_3 \\ \delta & \delta & \delta_6 & \cdots & \delta \\ \vdots & \vdots & \vdots & \ddots & \vdots \\ \delta & \delta & \delta & \cdots & \delta_6 \end{bmatrix}. \tag{73}$$

It can be noticed that δ_3, δ_4, δ_5, and δ_6 are different from those in the symmetrical condition, where

$$\delta_3=\frac{M}{M-L-Dev_2\cdot M}, \tag{74}$$

$$\delta_4=\frac{(Dev_2+1)LM+[(n-3)\cdot Dev_2-1]M^2}{(L-M)(M-L+M\cdot Dev_2)}, \tag{75}$$

$$\delta_5=\frac{L+(n-2)M}{L-(Dev_2+1)M}, \tag{76}$$

$$\delta_6=\frac{[L+(n-2)M](L-M+M\cdot Dev_2)-2M^2\cdot Dev_2}{(L-M)(L-M+Dev_2\cdot M)}. \tag{77}$$

2) Effect of Mutual Inductance Deviation on Transient Performances: The equivalent common-mode transient inductance

of each phase of the MCCI is equal to the pseudodecoupled inductance. Therefore, the common-mode transient inductance of each phase of the MCCI with self-inductance deviation can also be calculated by (69) and (70).

The variation in pseudodecoupled inductances (also the common-mode transient inductances) of phase 1 and phase 2 due to mutual inductance deviation Dev_2, relative to the symmetrical condition, can be calculated by (78) shown at the bottom of this page. The variation in pseudodecoupled inductances (also the common-mode transient inductances) of the remaining phases relative to the symmetrical condition can be calculated by (79) shown at the bottom of this page. The variation in equivalent transient inductance of the PCC relative to the symmetrical condition can be calculated by (80) shown at the bottom of this page

Fig. 7, based on (78), (79), and (80), illustrates the effect of the mutual inductance deviation Dev_2 on pseudodecoupled inductance parameters. Comparing Figs. 6 and 7, it can be observed that the mutual inductance deviation Dev_2 has less effect on the pseudodecoupled inductance parameters compared to the self-inductance deviation Dev_1, and the effect is opposite. In the case of inverse coupling, a positive mutual inductance deviation Dev_2 reduces the pseudodecoupled inductance of each phase and the equivalent transient inductance at the PCC. As the mutual inductance deviation Dev_2 increases, the reduction in the pseudodecoupled inductance of each phase and the equivalent transient inductance at the PCC becomes more pronounced. The greater the number of phases n, the smaller the effect of the mutual inductance deviation, but this effect becomes less pronounced after 20 phases. In the case of inverse coupling, the tighter the coupling, the greater the effect of the deviation, which becomes significant after the coupling coefficient α reaches -0.8.

For the equivalent differential mode transient inductance, combining (6), (68), and (73), it can be seen that the mutual inductance deviation causes the differential mode transient inductance from phase 1 to phase 2 and that from phase 2 to phase 1 to be unequal to differential mode transient inductance L_{dtr}^{Dev2} between the remaining phases, as shown in

$$L_{\mathrm{dtr12}}^{Dev2} = \frac{L_{\mathrm{dp1}}^{Dev2}}{\delta_5 - \delta_4} = L_{\mathrm{dtr21}}^{Dev2} = \frac{L_{\mathrm{dp2}}^{Dev2}}{\delta_5 - \delta_4}. \tag{81}$$

$$L_{\mathrm{dtr}}^{Dev2} = \frac{L_{\mathrm{dp}}^{Dev2}}{\delta_6 - \delta}. \tag{82}$$

3) Effect of Mutual Inductance Deviation on Steady-State Performances: Substituting (68) and (73) into (27), the peak-to-peak value of current ripples of phases 1 and 2 of the MCCI with the mutual inductance deviation Dev_2 can be calculated as follows:

$$\begin{aligned}\Delta i_{\mathrm{cp1}(Dev2)}^{\mathrm{pp}} &= \Delta i_{\mathrm{cp2}(Dev2)}^{\mathrm{pp}} \\ &= \frac{L_{\mathrm{dp}}^{\mathrm{sym}}}{L_{\mathrm{dp}}^{Dev2}} \Delta i_{\mathrm{dp}}^{\mathrm{pp}} \left[n\delta_3 \cdot F_c + \left(\delta_5 \frac{1}{1 + Dev_{\mathrm{dp2}}} - \delta_3 \right) \right. \\ &\quad \left. + \gamma_{12} \cdot \left(\delta_4 \frac{1}{1 + Dev_{\mathrm{dp2}}} - \delta_3 \right) \right]\end{aligned} \tag{83}$$

where γ_{12} depends on the phase difference between the PWM of phase 1 and phase 2. Compared to the phase current ripple in the MCSCI, the current ripple in phase 1 or phase 2 of the MCCI with the mutual-inductance deviation has an additional triangular wave component. Thus, it is similar to the phase current ripple of the MCCI with the self-inductance deviation shown in Fig. 8.

Similarly, the the peak-to-peak value of current ripple $\Delta i_{\mathrm{cp}i(Dev2)}^{\mathrm{pp}}$ for phase i ($i \neq 1$ & $i \neq 2$) is calculated as follows:

$$\begin{aligned}\Delta i_{\mathrm{cp}i(Dev2)}^{\mathrm{pp}} = \frac{L_{\mathrm{dp}}^{\mathrm{sym}}}{L_{\mathrm{dp}}^{Dev2}} \Delta i_{\mathrm{dp}}^{\mathrm{pp}} \left[n\delta \cdot F_c + (\delta_6 - \delta) \right. \\ \left. + (\gamma_{1i} + \gamma_{2i}) \cdot \delta \frac{-Dev_{\mathrm{dp2}}}{1 + Dev_{\mathrm{dp2}}} \right]\end{aligned} \tag{84}$$

where γ_{1i} depends on the phase difference between the PWM of phase 1 and phase i, γ_{2i} depends on the phase difference the PWM of phase 2 and phase i. Compared to the phase current ripple in the MCSCI, the current ripple in phase i of the MCCI with the mutual-inductance deviation has two additional triangular waveform components.

The peak-to-peak value of current ripple $\Delta i_{\mathrm{pcc}(Dev2)}^{\mathrm{pp}}$ at the PCC can be calculated by the following equation:

$$\Delta i_{\mathrm{pcc}(Dev2)}^{\mathrm{pp}} = n\Delta i_{\mathrm{dp}}^{\mathrm{pp}} \cdot \left(F_c - \frac{(1 + \gamma_{12})\, Dev_{\mathrm{dp2}}}{n\,(1 + Dev_{\mathrm{dp2}})} \right) \tag{85}$$

where γ_{12} depends on the phase difference between the PWM of phase 1 and phase 2. Similar to the phase current ripple of MCCI with self-inductance deviation shown in Fig. 8, the current ripple at the PCC of the MCCI with mutual-inductance deviation has two more triangular waveform components than the current ripple at the PCC in the MCSCI. Since there are two additional triangular waveform components, when the phase difference of these components is appropriate, the ripple reduction effect of the current at the PCC will be close to that in the MCSCI.

$$L_{\mathrm{dp1}}^{Dev2}/L_{\mathrm{dp}}^{\mathrm{sym}} = L_{\mathrm{dp2}}^{Dev2}/L_{\mathrm{dp}}^{\mathrm{sym}} = \frac{(1+\alpha)\,(1-\alpha/\,(n-1) + \alpha Dev_2/\,(n-1)) - 2\alpha^2 Dev_2/\,(n-1)^2}{(1-\alpha/\,(n-1))\,(1+\alpha)} \tag{78}$$

$$L_{\mathrm{dp}}^{Dev2}/L_{\mathrm{dp}}^{\mathrm{sym}} = \frac{(1+\alpha)\,(1-\alpha/\,(n-1) + \alpha Dev_2/\,(n-1)) - 2\alpha^2 Dev_2/\,(n-1)^2}{(1+\alpha)\,(1-\alpha/\,(n-1) + \alpha Dev_2/\,(n-1))} \tag{79}$$

$$L_{\mathrm{tr_{pcc}}}^{Dev2}/L_{\mathrm{tr_{pcc}}}^{\mathrm{sym}} = \frac{n[(1+\alpha)\,(1-\alpha/\,(n-1) + \alpha Dev_2/\,(n-1)) - 2\alpha^2 Dev_2/\,(n-1)^2}{(1+\alpha)\,[n\,(1-\alpha/\,(n-1) + \alpha Dev_2/\,(n-1)) - 2\alpha Dev_2/\,(n-1)]} \tag{80}$$

Accordingly, at this case $\mu_{\rm pcc}$ is

$$\mu_{\rm pcc} = \frac{F_c - \frac{(1+\gamma)Dev_{\rm dp1}}{n(1+Dev_{\rm dp1})}}{1 - \frac{2Dev_{\rm dp1}}{n(1+Dev_{\rm dp1})}}. \tag{86}$$

The above discussion is based on the example of self-inductance or mutual inductance deviation in a particular phase. For the case of multiphase self-inductance or mutual inductance deviation, the effects caused by the self-inductance and mutual-inductance deviation of each phase can be discussed individually and then superimposed. Alternatively, (3), (6), (27), and (31) can be used directly by substitute the inductance matrix for discussions.

D. Design Ideas for Coupled Inductors With Asymmetries

Based on the previous analysis of the MCCI, the coupled inductor can be designed according to the following recommendations:

1) Asymmetrical Coupled Inductor Compensation Design Ideas: From the previous analysis, it can be seen that even in the case of asymmetrical self-inductance and mutual inductance, the consistent pseudodecoupled inductance of each phase can make the current ripple at the PCC the same as in the symmetrical case. In addition, the consistent pseudodecoupled inductance of each phase ensures that each phase has the same common-mode transient characteristics. The asymmetry of self-inductance or mutual-inductance parameters of coupled inductors due to core structure design problems or other factors can be compensated appropriately to make their pseudodecoupling inductance consistent.

Based on the quantitative analysis presented in this section, the compensation strategy is discussed using a three-phase coupled inductor as an example, as follows:

If the coupling inductor is inverse-coupled, and there is a negative deviation in the mutual inductance of phases 1 and 3, then theoretically the pseudodecoupled inductances of phase 1 and phase 3 will be larger compared to phase 2. It is possible to increase the self-inductance of phase 2, e.g., by increasing the number of turns or by connecting a small inductor in series with phase 2, so that the pseudodecoupled inductances of all three phases can be as consistent as possible. If there is a positive deviation, then the pseudodecoupled inductances of phase 1 and phase 3 will be smaller, and the self-inductances of phases 1 and 3 can be increased appropriately to make the pseudodecoupled inductances as consistent as possible.

If the coupling inductor is positive-coupled, and there is a negative deviation in the mutual inductance of phases 1 and 3, then theoretically the pseudodecoupled inductances of phase 1 and phase 3 will be smaller compared to that of phase 2. In this case, the self-inductances of phases 1 and 3 can be increased appropriately. If there is a positive deviation, then the pseudodecoupled inductances of phase 1 and phase 3 will be larger, and the self-inductance of phase 2 can be increased appropriately to make the pseudodecoupled inductances as consistent as possible.

2) Selection of Coupling Coefficient: In the case of MCSCI, the tighter the coupled inductors are inverse-coupled, the better the steady-state and transient performance of the converter. However, as analyzed in this section, excessively tight inverse coupling amplifies the effects of self-inductance or mutual-inductance deviations, causing the performance of the MCCI to differ significantly from expectations. Therefore, based on the analysis in Figs. 6 and 7, it is conservatively recommended that the coupling coefficient should not be less than -0.8.

IV. Control Strategies for PWM Phase-Shift and Phase Sequence of Multiphase Converters With Asymmetrical Coupled Inductors

From the analysis in Section II, we know that the MCCI and its pseudodecoupled circuit have the same transient and steady-state characteristics at the PCC under CCM condition. In addition, the proposed pseudodecoupling method enables a quantitative analysis of the effect of PWM phase shift and phase sequence on current ripple. This makes feasible to extend the PWM phase-shift and phase-sequence control strategy, which is applied to multiphase converters with independent inductors, to MCCI. This section validates this idea and develops the optimal control strategies for MCCI PWM phase shift and phase sequence.

A. Control Strategy for PWM Phase Shift

Regarding phase-shift control strategies for multiphase converters with independent inductors, Caris et al. [27], [28] proposed a method to calculate improved carrier phase-shifts that completely remove the fundamental switching frequency subharmonic components from the output current spectrum. It was verified that although the higher harmonic components of the ripple increase slightly when the fundamental component is removed, the overall reduction in ripple magnitude is greater.

For a independent inductor multiphase converter, the ripple at the PCC can be regarded as consisting of n triangular waveforms. The fundamental component of each triangle waveform can be expressed as a phasor

$$\widetilde{I}_k = A_k e^{j(\varphi_k + \omega t)} \tag{87}$$

where $\widetilde{I}_k$ represents the fundamental component phasor of the kth triangular waveform, and the amplitude of this phasor, represented as A_k.

As shown in Fig. 9, the phasor representation of the strategy is demonstrated using a three-phase converter as an example. For a three-phase converter, the phasor can be adjusted using the cosine theorem as follows:

$$\begin{aligned}\varphi_2' &= \pi - \arccos\left(\left(A_1^2 + A_2^2 - A_3^2\right)/(2A_1A_2)\right)\\ \varphi_3' &= \pi + \arccos\left(\left(A_3^2 + A_1^2 - A_2^2\right)/(2A_1A_3)\right).\end{aligned} \tag{88}$$

For converters which $n > 3$, the optimal phase-shift strategy can be solved using numerical methods such as Newton's iterative method.

According to (31), the current ripple at the PCC of an MCCI can be regarded as consisting of *n* triangular waveforms, allowing the strategy to be applied similarly. To make this strategy applicable to optimise the ripple at the PCC of an MCCI, since

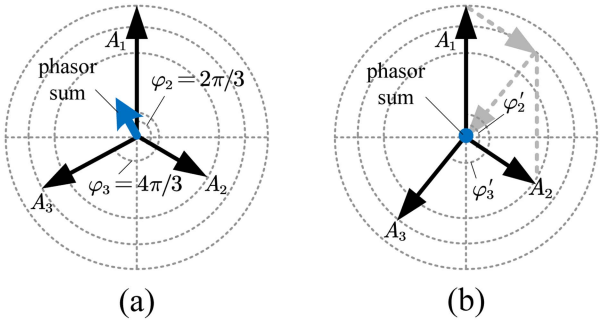

Fig. 9. Phasor representation when changing the PWM phase shift (Taking a three-phase as an example.) (a) Before changing the PWM phase shift. (b) After changing the PWM phase shift.

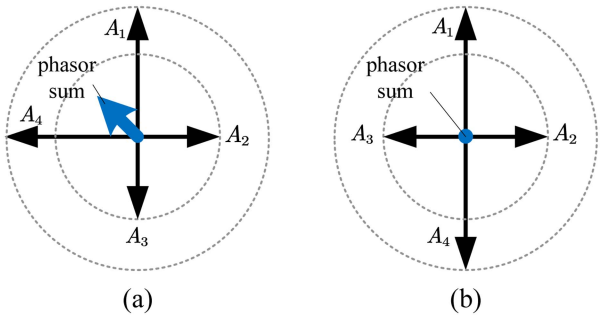

Fig. 10. Phasor representation when changing the phase sequence (Taking a four-phase as an example.) (a) Before changing the PWM phase sequence. (b) After changing the PWM phase sequence.

the triangular waveform that makes up the ripple of the PCC of an MCCI is determined by the pseudodecoupled inductance of each phase, it is sufficient to revise the expression of each triangle waveform phasor. A Fourier analysis of (31) is performed and the amplitude expression is modified as follows:

$$A_k = \frac{2V_{\mathrm{h}}}{L_{\mathrm{dp}_k} f_{\mathrm{sw}} (1 - D_k) \pi^2} \sin(D_k \pi). \tag{89}$$

If applied to reduce the phase current ripple, since the triangular waveform that makes up the MCCI phase current ripple is determined by both the pseudodecoupled inductance of that phase and the ripple distribution coefficient, the amplitude expression is modified as follows:

$$A_k = \frac{2\delta_{ik} V_{\mathrm{h}}}{L_{\mathrm{dp}_k} f_{\mathrm{sw}} (1 - D_k) \pi^2} \sin(D_k \pi). \tag{90}$$

B. Control Strategy for PWM Phase Sequence

For a phase sequence control strategy for independent inductor multiphase converters, Garcia et al. [26] proposed a method of ripple reduction using digital control. This method is based on the idea that if each pair of phases with the most similar ripples are shifted by 180°, the ripples in the total current will be minimized. Fig. 10 shows the phasor representation of the strategy. In Fig. 10(b), two phasors of similar size are shifted by 180°, resulting in a significant reduction of the phasor sum compared to Fig. 10(a). This strategy allows for quickly obtaining a better phase sequence with lower computational power, though it may not necessarily be optimal.

For this strategy to be applied to a coupled inductor multiphase converter, the amplitude can be calculated through (89) or (90).

To obtain the optimal phase sequence of MCCI, the optimization problem can be defined as detailed in Appendix B. Since the PWM phase sequence optimization problem involves sequences, it has nonpolynomial level complexity. Therefore, using a heuristic algorithm is recommended to solve it. Fig. 11 shows the genetic algorithm used to solve for the optimal phase sequence.

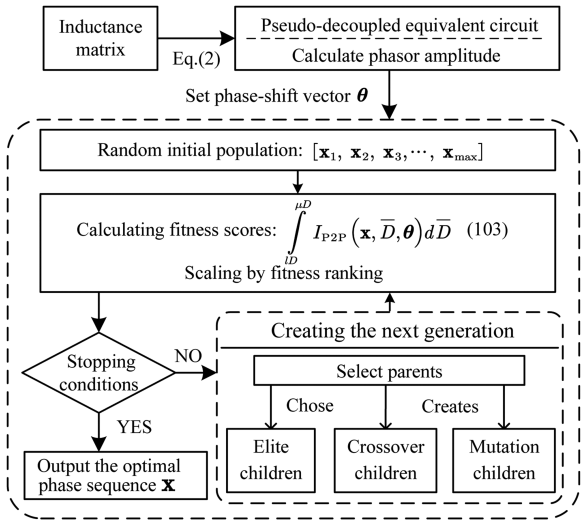

Fig. 11. Genetic algorithm implementation for the optimal phase sequence.

TABLE I
INDUCTOR PARAMETERS USED FOR CASE STUDIES AND SIMULATIONS

Coupled Inductor A (μH)					
L_{A1}	L_{A2}	L_{A3}	M_{A12}	M_{A23}	M_{A13}
99.353	109.152	102.257	-28.49	-28.9215	-13.314
Coupled Inductor B (μH)					
L_{B1}	L_{B2}	L_{B3}	M_{B12}	M_{B23}	M_{B13}
131.25	171.22	136.605	-34.4075	-37.3205	-13.202

C. Case Study: Six-Phase Boost Converter

To illustrate how the performance of an MCACI can be improved using an optimized PWM phase sequence and phase control strategy, a case study of a six-phase Boost converter is performed. The topology of this six-phase Boost converter is shown in Fig. 12. The converter consists of two three-phase coupled inductors, labeled as Coupled Inductor A and Coupled Inductor B. Coupled Inductor A is shared by phase A1, phase A2, and phase A3, while Coupled Inductor B is shared by phase B1, phase B2, and phase B3. The inductor parameters used for the case study are shown in Table I.

The following two cases will be discussed separately: First, we will take a three-phase operation as an example to discuss

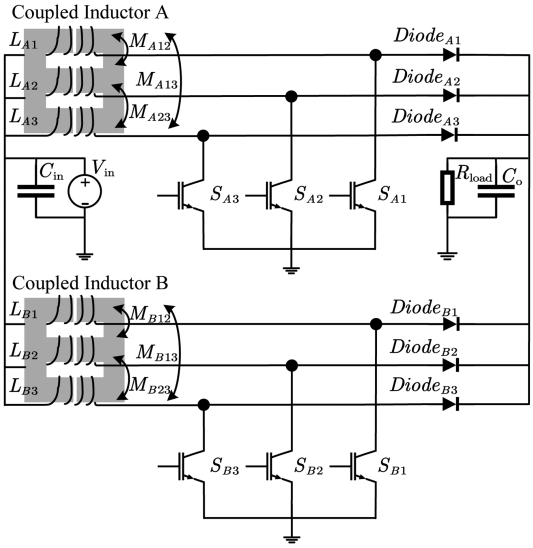

Fig. 12. Six-phase Boost converter topology used for case study and simulation.

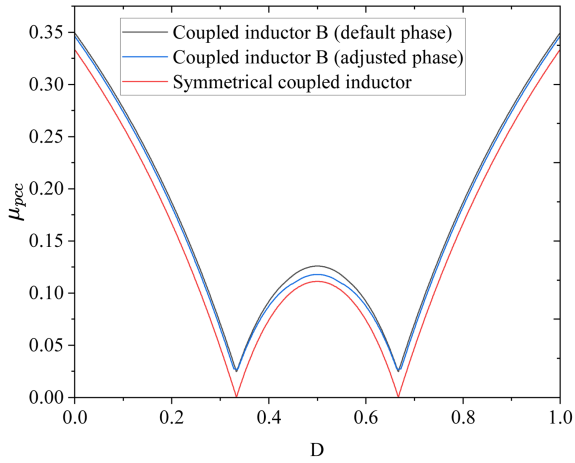

Fig. 13. Performance improvement coefficient $\mu_{\rm pcc}$ after phase adjusted under three-phase operation mode.

TABLE II
PWM PHASE SHIFT OF B1, B2, AND B3 UNDER THREE-PHASE OPERATION MODE

Converter Phase	PWM Sequence	Pseudo-decoupled Inductance (μH)	Phase Shift (Default)	Phase Shift (Adjusted)
B1	1th	86.67	0	0
B2	2th	94.07	$2\pi/3$	$0.6520\,\pi$
B3	3th	88.19	$4\pi/3$	$1.3076\,\pi$

TABLE III
PWM PHASE SEQUENCE UNDER SIX-PHASE OPERATION MODE

Converter Phase	Pseudo-decoupled Inductance (μH)	Sequence (Default)	Sequence (Empirical)	Sequence (Optimized)
A1	56.7	1th(0)	1th(0)	1th(0)
A2	54.53	2th $\left(\frac{1\pi}{3}\right)$	5th $\left(\frac{4\pi}{3}\right)$	5th $\left(\frac{4\pi}{3}\right)$
A3	57.93	3th $\left(\frac{2\pi}{3}\right)$	3th $\left(\frac{2\pi}{3}\right)$	3th $\left(\frac{2\pi}{3}\right)$
B1	86.67	4th $\left(\frac{3\pi}{3}\right)$	2th $\left(\frac{1\pi}{3}\right)$	2th $\left(\frac{1\pi}{3}\right)$
B2	94.07	5th $\left(\frac{4\pi}{3}\right)$	4th $\left(\frac{3\pi}{3}\right)$	6th $\left(\frac{5\pi}{3}\right)$
B3	88.19	6th $\left(\frac{5\pi}{3}\right)$	6th $\left(\frac{5\pi}{3}\right)$	4th $\left(\frac{3\pi}{3}\right)$

the effect of changing the PWM phase shift on converter performance. Second, we will take a six-phase operation as an example to discuss the effect of changing the PWM phase sequence on the converter performance.

In the analysis, the duty cycle of each phase is kept the same and set to D. The performance of the converter is evaluated using the performance improvement coefficient $\mu_{\rm pcc}$, which is defined by (34).

1) Effect of PWM Phase Shift on The Performance: Similar to the independent inductor multiphase converter [27], [28], the three-phase converter is sufficient to verify the effect of phase-shift change on the current ripple of MCACI. Therefore, the three-phase operation mode (phase B1, phase B2, and phase B3) is used for illustration. The PWM phase-shift strategy is shown in Table II and the comparison results are shown in Fig. 13.

The default phase-shift strategy of PWM is that the initial phase-shift of each phase differs by $2\pi/3$ in turn, so the PWM phase shifts of phase B1, phase B2, phase B3 are 0, $2\pi/3$, $4\pi/3$, respectively. Whereas the adjusted PWM phase shift is calculated based on (90).

It can be seen from Fig. 13 that the phase-shift-adjusted $\mu_{\rm pcc}$ curves are closer to the symmetrical three-phase converter, indicating that the current ripple at the PCC of the converter is reduced after phase shift adjustment.

2) Effect of PWM Sequence on The Performance: Since an MCACI with a number of phases greater than three is required to discuss the effect of phase sequence, the six-phase operation mode is used for illustration. We compare the effect of three sequences on the performance improvement $\mu_{\rm pcc}$ at the PCC under the condition that the phases shift differ sequentially by $\pi/6$. The PWM phase-sequencing strategies are shown in Table III, and the calculation and simulation results of the comparison are shown in Fig. 14. The parameters of the converter used in the simulation are given in Table VIII.

The default phase sequence of the PWM, i.e., the inductor layout order of Fig. 12, has the phase sequence 1, 2, 3, 4, 5, and 6 in sequence. The empirical control PWM phase sequence is 1, 5, 3, 2, 4, 6, which is summarized by an experienced engineer. The optimal phase sequence of the PWM obtained through optimization analysis is 1, 5, 3, 2, 6, 4. The definition of the optimization problem is detailed in Appendix B. In this case study, a simplified objective function is chosen and MATLAB's "ga" function is used for the solution, with the strategy and most of the parameters of the genetic algorithm kept at default settings. Fig. 14 shows that the converter with optimal phase sequence outperforms the empirical phase sequence when the duty cycle D is in the range of $1/6$–$5/6$, and significantly outperforms the default phase sequence in the full duty cycle range. Although there are some gaps in performance compared to the ideal symmetrical converter, the performance of the MCACI with optimal phase sequence is the closest to the ideal symmetrical

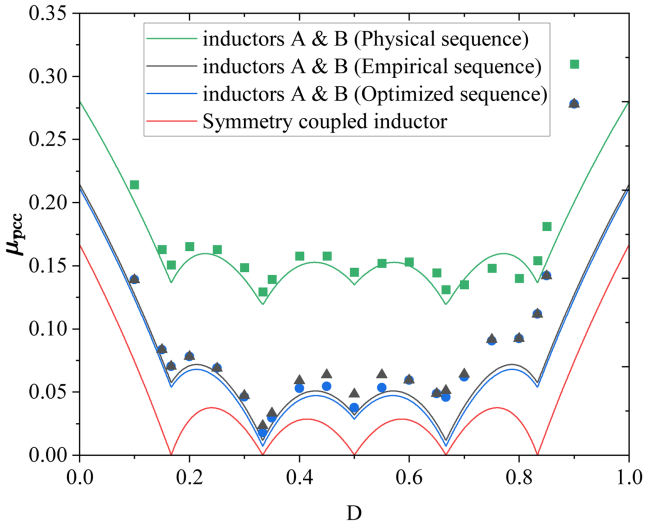

Fig. 14. Performance improvement coefficient μ_{pcc} of calculation and simulation under six-phase operation mode with different PWM phase sequences (The lines are the calculation results and the scatter points are the simulation results.)

converter. The simulation results are generally consistent with the theoretical calculations, showing similar trends. However, at higher duty cycles, a noticeable discrepancy appears between the simulation and theoretical results. This difference arises because, at higher duty cycles, the increased current causes a significant deviation of the inductor voltage waveform from the ideal rectangular shape, which differs from the assumption made in theoretical calculations.

D. Discussion of the Control Strategies

This section discusses the idea of extending the PWM phase-shift and phase-sequence control strategies to MCACIs. From the perspective of developing control strategies for MCCI, it is essential not only to adjust phase shift and phase sequence, but also to address current balancing. In multiphase converters with independent inductors, nonlinear inductor effects play a crucial role in achieving current balancing. Previous studies, such as [32], have demonstrated the potential of leveraging these nonlinear characteristics for improved balancing performance. However, a deeper understanding of the nonlinear dynamics of hypothetical pseudo-decoupled inductors and their impact on current balancing remains necessary to achieve effective current balancing in MCCI. These aspects, while important, fall beyond the scope of this article and will be explored in future work.

V. Experimental and Simulation Verification

A. Experimental Platform Setup

Fig. 15 illustrates the coupled inductors and the interleaved six-phase boost converter used for the experiment. This converter was developed for high-power onboard hydrogen fuel cell applications. The main parameters of the converter are shown in Table IV.

The converter consists of two three-phase coupled inductors, labeled as Coupled Inductor A and Coupled Inductor B. Coupled

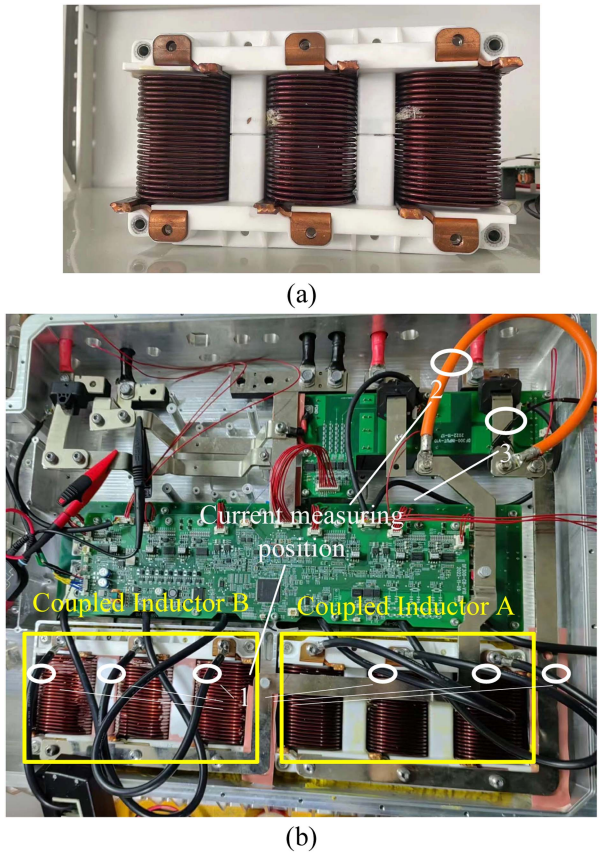

Fig. 15. Hardware platform. (a) Coupled inductor. (b) Six-phase boost converter.

TABLE IV
Experimental Parameters of the Converter Prototype

Parameters	Value
Input Voltage (V_{in})	250 V
Switching Frequency (f_{sw})	18 kHz
Phase Number (n)	3 or 6
Input Capacitance (C_{in}) / Output Capacitance (C_{o})	100 μF / 100 μF
IGBT Equivalent On-resistance	0.004 Ω
Diode Equivalent On-resistance	0.0045 Ω
Diode Forward Voltage Drop	2 V

Inductor A is shared by phase A1, phase A2, and phase A3, while Coupled Inductor B is shared by phase B1, phase B2, and phase B3. The inductor's core is MKF212U35-90.5 from EAGTOP company. The parameters of these two inductors are not consistent due to the production lot, and each inductor itself is asymmetrical in each phase parameter. The Agilent 4263B LCR meter is used to measure the self-inductance, mutual inductance, and equivalent series resistance of coupled inductors A and B. The inductance measurement parameters are shown in Table V. The pseudodecoupled inductance of each phase of the Boost converter is calculated according to the coupled inductor parameters in Table V and (3) as shown in Table VI.

A Tektronix TCP303 current probe with a TCPA300 amplifier was used to measure the inductor currents (including dc and ac components) of each phase at position 1. A TCP404XL current probe with a TCPA400 amplifier was used to measure the total

TABLE V
MEASUREMENT PARAMETERS OF THE COUPLED INDUCTORS

Coupled Inductor A		
L_{A1}	L_{A2}	L_{A3}
99.453 μH	109.252 μH	102.257 μH
M_{A12}	M_{A23}	M_{A13}
-28.49 μH	-28.9215 μH	-13.314 μH
R_{A1}	R_{A2}	R_{A3}
0.1563 Ω	0.1112 Ω	0.1651 Ω
Coupled Inductor B		
L_{B1}	L_{B2}	L_{B3}
131.25 μH	171.22 μH	136.605 μH
M_{B12}	M_{B23}	M_{B13}
-34.4075 μH	-37.3205 μH	-13.202 μH
R_{B1}	R_{B2}	R_{B3}
0.2035 Ω	0.3908 Ω	0.2143 Ω

TABLE VI
CALCULATED PSEUDODECOUPLED INDUCTANCE FOR EACH PHASE

$L_{\mathrm{dp}(A1)}$	$L_{\mathrm{dp}(A2)}$	$L_{\mathrm{dp}(A3)}$	$L_{\mathrm{dp}(B1)}$	$L_{\mathrm{dp}(B2)}$	$L_{\mathrm{dp}(B3)}$
56.70 μH	54.53 μH	57.93 μH	86.67 μH	94.07 μH	88.19 μH

input current (including dc and ac components) of phases B1, B2, and B3 at position 2. A CWT Rogowski coil from PEM was used to measure the total input current ripple (ac components) of the 6 phases at position 3. According to the datasheet, the insertion impedance of these probes is 4 to 5 orders of magnitude smaller than the impedance of the coupled inductors used, which is negligible. Voltage measurements were made using Tektronix P5200A probes.

The experiments were carried out under open-loop conditions. Two types of loads were used for the experiments, as shown in Fig. 16, using a dc power supply as a 500-V constant voltage load and six 50 Ω resistors in parallel as a resistive load.

B. Verification of Steady-State Performance Analysis for MCCI

1) Steady-State Experiment With the Same Inductor Voltage for Each Phase: According to the analysis in Section II, when the same (same phase-shift, duty cycle, and amplitude) rectangular waveform voltage is applied to each phase of MCCIs, the equivalent steady-state inductance of each phase is equal to the pseudodecoupled inductance. In this experiment, the converter was operated under the three-phase operation mode of phase A1, phase A2, and phase A3 and the three-phase operation mode of phase B1, phase B2, and phase B3, respectively, with the constant voltage load. The PWM phase shift of each phase was set to 0, and the duty cycle of each phase was set to 0.505. The current and voltage waveforms are shown in Fig. 17. The experimental results and the theoretical steady-state inductance are shown in Table VII(a), where the theoretical

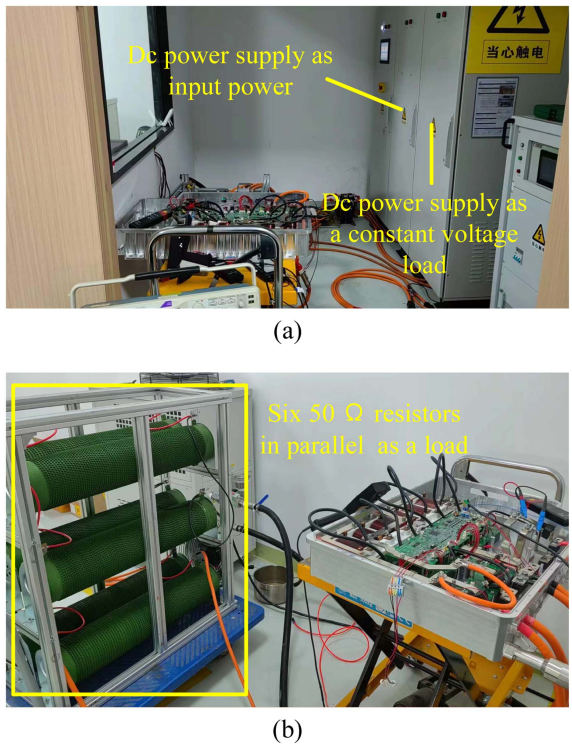

Fig. 16. Two types of loads used in the experiment: (a) DC power supply as a 500-V constant voltage load; (b) six 50 Ω resistors in parallel as resistive loads.

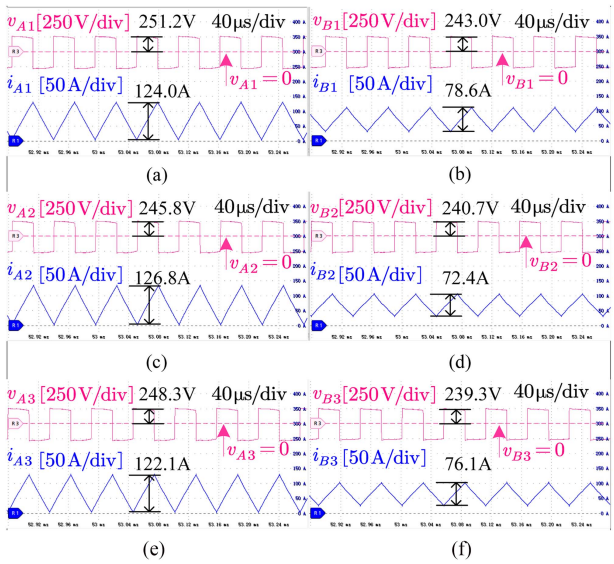

Fig. 17. Experimental steady-state voltage and current waveforms under the same inductor voltage setting ($D_{A1} = D_{A2} = D_{A3} = 0.505$, $D_{B1} = D_{B2} = D_{B3} = 0.505$, constant voltage load): (a) inductor voltage and current of phase A1; (b) inductor voltage and current of phase B1; (c) inductor voltage and current of phase A2; (d) inductor voltage and current of phase B2; (e) inductor voltage and current of phase A3; (f) inductor voltage and current of phase B3.

steady-state inductance values are the pseudo-decoupled inductance values in Table VI.

Comparing the experimental steady-state inductances and the theoretical steady-state inductances shown in Table VII(a), it can

TABLE VII
EXPERIMENTAL RESULTS

(a) Steady-State Behavior with Same Inductor Voltage for Each Phase (D_{A1}=D_{A2}=D_{A3}=0.505, D_{B1}=D_{B2}=D_{B3}=0.505, Constant Voltage Load)

Phase of the Converter	Inductor High-level Voltage	Experimental Current Ripple	Experimental Steady-state Inductance	Theoretical Steady-state Inductance
A1	251.2 V	124.0 A	56.8 μH	56.7 μH
A2	245.8 V	126.8 A	54.4 μH	54.5 μH
A3	248.3 V	122.1 A	57.1 μH	57.9 μH
B1	243.0 V	78.6 A	86.7 μH	86.7 μH
B2	240.7 V	72.4 A	93.3 μH	94.1 μH
B3	239.3 V	76.1 A	88.2 μH	88.2 μH

(b) Steady-State Behavior with Same PWM Duty Cycle for Each Phase (D_{B1}=D_{B2}=D_{B3}=0.5, Resistive Load)

Phase of the Converter	Inductor High-level Voltage	Experimental Current Ripple	Theoretical Current Ripple
B1	240.9 V	47.6 A	48.0 A
B2	240.3 V	35.8 A	35.7 A
B3	241.3 V	45.9 A	46.2 A
Input	240.8 V	27.8 A	28.2 A

(c) Transient Behavior under Common-Mode Perturbation (D_{B1}=D_{B2}=D_{B3}=0.5 to D_{B1}=D_{B2}=D_{B3}=0.6, Resistive Load)

Phase of the Converter	Cycle Avg Voltage Increment	Cycle Avg Current Increment	Experimental Transient Inductance	Theoretical Transient Inductance
B1	43.5 V	27.9 A	86.6 μH	86.7 μH
B2	44.2 V	25.7 A	95.6 μH	94.1 μH
B3	43.6 V	27.0 A	89.7 μH	88.2 μH

(d) Transient Behavior under Differential Mode Perturbation (D_{B1}=0.5 to D_{B1}=0.6,D_{B2}=D_{B3}=0.5, Resistive Load)

Phase of the Converter	Cycle Avg Voltage Increment	Cycle Avg Current Increment	Experimental Transient Inductance	Theoretical Transient Inductance
B1	50.2 V	23.1 A	-	-
B2	-	5.5 A	-	-
B3	-	3.7 A	-	-
input	-	31.8 A	87.7 μH	86.7 μH
B1-B2	-	17.6 A	158.5 μH	158.4 μH
B1-B3	-	19.4 A	143.7 μH	144.2 μH

(e) Verification of PWM phase-shift adjustment method (D_{B1}=D_{B2}=D_{B3}=0.5, Constant Voltage Load)

Phase-shift Strategy	Input Current Ripple
Default	27.4 A
adjusted	26.0 A

(f) Verification of PWM phase sequence adjustment method (D_{A1}=D_{A2}=D_{A3}=D_{B1}=D_{B2}=D_{B3}=0.5, Constant Voltage Load)

Phase Sequence Strategy	Input Current Ripple
Default	89.6 A
Empirical	23.2 A
Optimized	18.0 A

be found that they are very close, which verifies the theoretical analysis in Section II.

2) Steady-State Experiment With the Same PWM Duty Cycle for Each Phase: Section II provides the formulas for calculating the peak-to-peak values of inductor current ripple at steady state for each phase and at the PCC. In this experiment, the converter was operated under the three-phase operation mode of phase B1, phase B2, and phase B3, with the resistive load. The PWM phase shift of each phase differs by $2\pi/3$ in turn, and the duty cycle of each phase was set to 0.5. The current and voltage waveforms are shown in Fig. 18. The experimental results and the theoretical current ripple peak-to-peak values calculated according to (28), (32) are shown in Table VII(b).

TABLE VIII
SIMULATION PARAMETERS OF THE CONVERTER PROTOTYPE

Parameters	Value
Input Voltage (V_{in})	250 V
Switching Frequency (f_{sw})	18 kHz
Phase Number (n)	3
Input Capacitance (C_{in}) / Output Capacitance (C_{o})	100 μF / 100 μF
IGBT Equivalent On-resistance	0.004 Ω
Diode Equivalent On-resistance	0.0045 Ω
Diode Forward Voltage Drop	2 V
Load Resistance (R_{load})	1 Ω

TABLE IX
SIMULATION RESULTS OF STEADY-STATE SIMULATION WITH DIFFERENT PWM DUTY CYCLES FOR EACH PHASE ($D_{B1} = 0.5$, $D_{B2} = 0.52$, $D_{B3} = 0.51$, $R_{\text{load}} = 1\ \Omega$)

Phase of the Converter	Inductor High-level Voltage [V]	Simulation Current Ripple [A]	Theoretical Current Ripple [A]
B1	248.4	48.5	48.8
B2	248.0	38.7	38.3
B3	249.5	49.2	49.1
Input	-	31.7	31.3

The difference between the experimental results and theoretical calculations under this experimental condition is within 2%. The error is acceptable considering the undesirable inductor voltage waveform and the accuracy of the measuring instruments (TCP303 dc gain accuracy is $\pm$ 3% and P5200A dc gain accuracy is $\pm$ 2%). Therefore, the experimental results validate the theoretical analysis of the steady-state current ripple in Section II.

3) Steady-State Simulation With Different PWM Duty Cycles for Each Phase: Due to the limitations of the experimental conditions, MATLAB is used to simulate the steady-state behavior of the converter at different duty cycle settings for each phase. The simulation topology is shown in Fig. 12. The parameters of the converter used in the simulation are given in Table VIII and the inductor parameters are given in Table I. In this simulation, the converter was operated under the three-phase operation mode of phase B1, phase B2, and phase B3, with a 1 Ω resistive load. The PWM phase shift of each phase differs by $2\pi/3$ in turn, and the duty cycles of phases B1, B2, and B3 are 0.5, 0.52, and 0.51, respectively. The current waveforms are shown in Fig. 19, and voltage waveforms are shown in Fig. 20.

The simulation results and the theoretical current ripple peak-to-peak values calculated according to (28), (32) are shown in Table IX. According to (28) and (32), the theoretical calculations of the peak-to-peak current ripple values of phase B1, phase B2, and phase B3 are 49.8 A, 37.2 A, and 47.8 A, respectively, and the peak-to-peak ripple value of the total input current is 29.3A. The simulation results in Fig. 19 show that the peak-to-peak current ripple values of phase B1, phase B2, and phase B3 are 48.5 A, 38.7 A, and 49.2 A, respectively, and the peak-to-peak ripple value of the total input current is 31.7 A.

There is some differences between theoretical and simulated values. This is due to the nonideal inductor voltage rectangular waveforms and the different inductor voltage high level averages

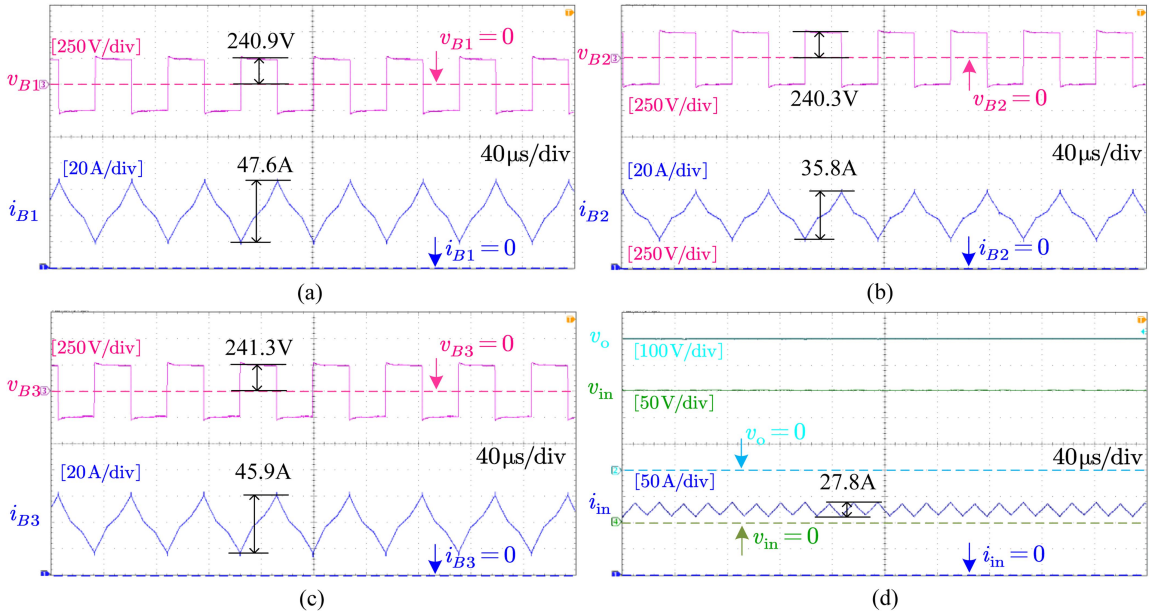

Fig. 18. Experimental steady-state voltage and current waveforms under the same PWM duty cycle setting ($D_{B1}=D_{B2}=D_{B3}=0.5$, resistive load): (a) inductor voltage and current of phase B1; (b) inductor voltage and current of phase B2; (c) inductor voltage and current of phase B3; (d) output voltage, input voltage, and input current.

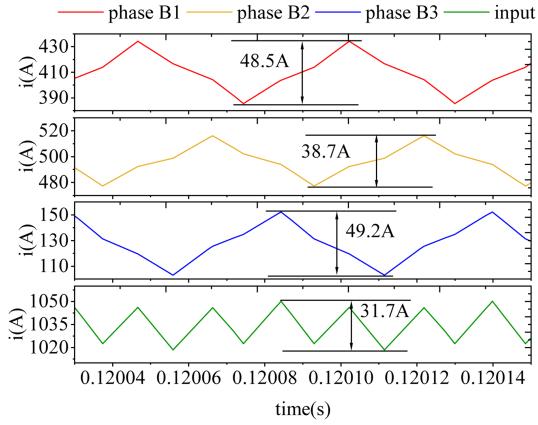

Fig. 19. Simulation steady-state current waveforms under the different PWM duty cycle setting ($D_{B1}=0.5$, $D_{B2}=0.52$, $D_{B3}=0.51$, $R_{\text{load}}=1\ \Omega$).

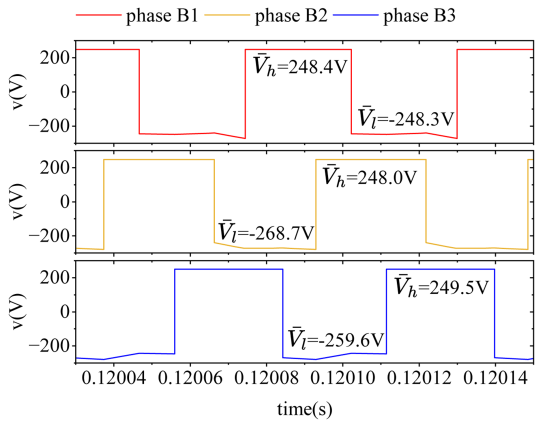

Fig. 20. Simulation steady-state voltage waveforms under the different PWM duty cycle setting ($D_{B1}=0.5$, $D_{B2}=0.52$, $D_{B3}=0.51$, $R_{\text{load}}=1\ \Omega$).

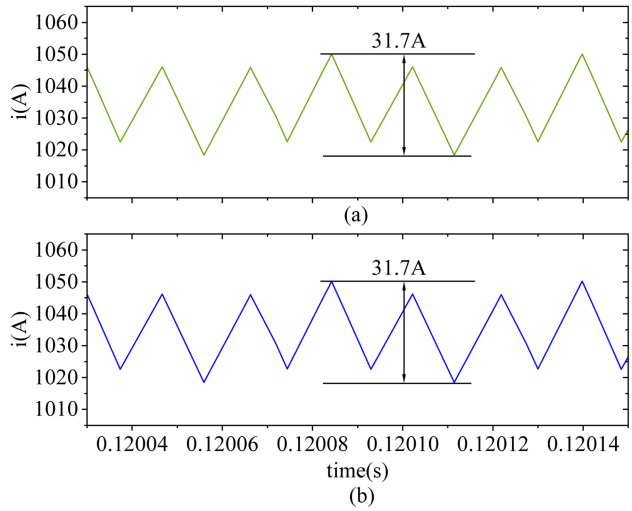

Fig. 21. Simulation input current waveforms of the converter and its pseudodecoupled circuit under the different PWM duty cycle setting ($D_{B1}=0.5$, $D_{B2}=0.52$, $D_{B3}=0.51$, $R_{\text{load}}=1\ \Omega$): (a) input current waveforms of the converter; (b) input current waveforms of its pseudodecoupled circuit.

for each phase as shown in Fig. 20, which caused by the fluctuations in output voltage and nonideal parameters of switching devices. So, (27) and (31) are revised as follows:

$$\Delta i_{\text{cp}_i}(t)=\frac{1}{f_{\text{sw}}}\sum_{j=1}^{n}\frac{V_{hj}D_j\delta_{ij}}{L_{\text{dp}_j}}f_j\left(t-\frac{\varphi_j}{2\pi}T_{\text{sw}}\right). \tag{91}$$

$$\Delta i_{\text{pcc}}(t)=\frac{1}{f_{\text{sw}}}\sum_{j=1}^{n}\frac{V_{hj}D_j}{L_{\text{dp}_j}}f_j\left(t-\frac{\varphi_j}{2\pi}T_{\text{sw}}\right) \tag{92}$$

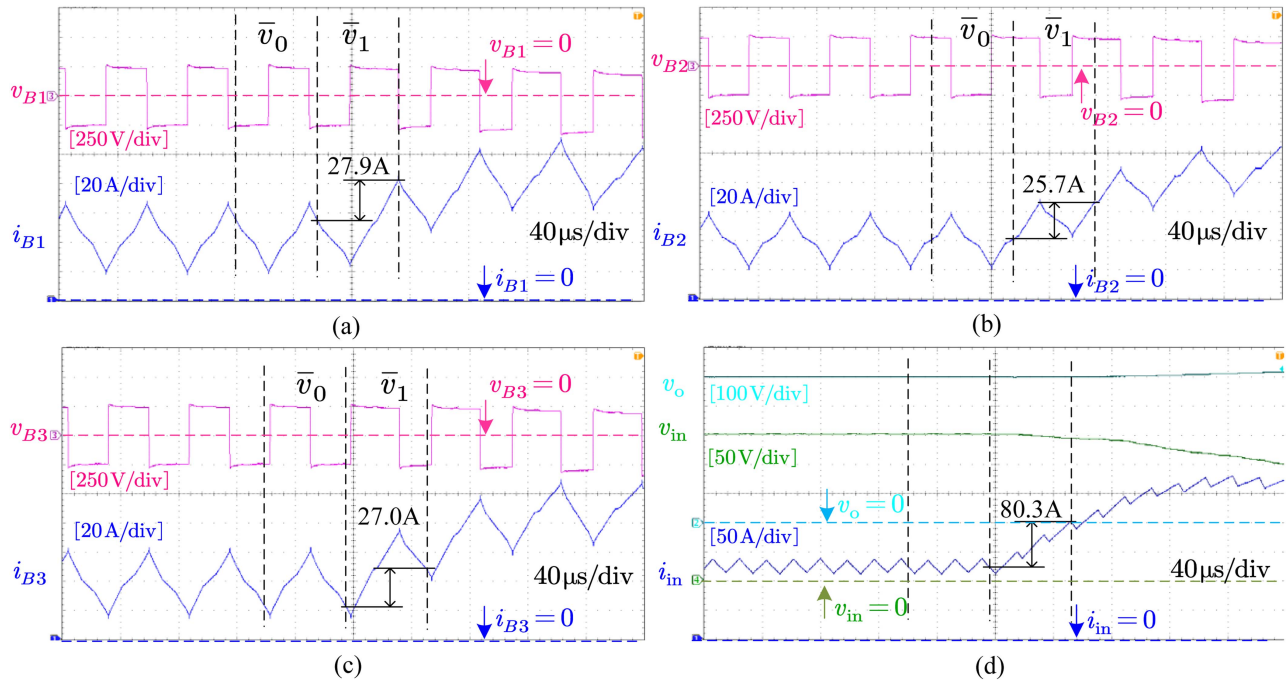

Fig. 22. Experimental voltage and current waveforms under common-mode duty cycle perturbation ($D_{B1}=D_{B2}=D_{B3}=0.5$ to $D_{B1}=D_{B2}=D_{B3}=0.6$, resistive load): (a) inductor voltage and current of phase B1; (b) inductor voltage and current of phase B2; (c) inductor voltage and current of phase B3; (d) output voltage, input voltage, and input current.

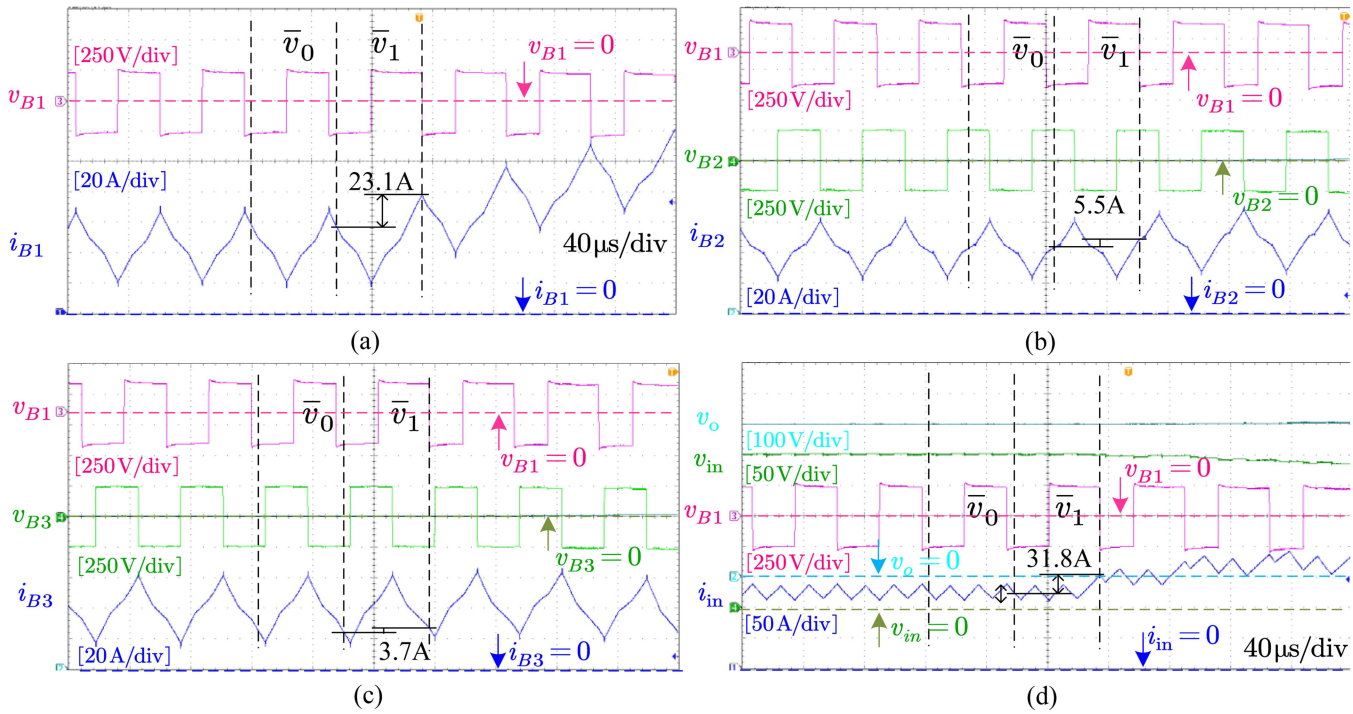

Fig. 23. Experimental voltage and current waveforms under differential mode duty cycle perturbation ($D_{B1}=0.5$ to $D_{B1}=0.6$, $D_{B2}=D_{B3}=0.5$ resistive load): (a) inductor voltage and current of phase B1; (b) inductor voltage of phase B1, inductor voltage and current of phase B2; (c) inductor voltage of phase B1, inductor voltage and current of phase B3; (d) output voltage, input voltage, inductor voltage of phase B1, and input current.

where V_{hj} is the inductor high-level voltage in phase j. Using the simulated inductor high-level voltage to calculate the peak-to-peak current ripple values of phase B1, phase B2, and phase B3 are 48.8 A, 38.3 A, and 49.1 A, respectively, and the peak-to-peak ripple value of the total input current is 31.3 A, which are consistent to the simulated values.

To further verify the accuracy of the modeling approach, the pseudodecoupled equivalent circuit of the converter is simulated. The inductance parameters are shown in the Table VI. The input currents of the coupled inductor Boost converter and its pseudodecoupled circuit under this operating condition are compared in Fig. 21. The current ripple shapes and peak-to-peak values of the two circuits are almost the same, which not only verifies the inference that the coupled-inductor Boost converter and its pseudodecoupled circuit have the same input current ripple, but also illustrates the versatility of the proposed pseudodecoupled circuit model—the pseudodecoupled circuit model is valid regardless of whether the inductor voltages are ideal rectangular waveform or not.

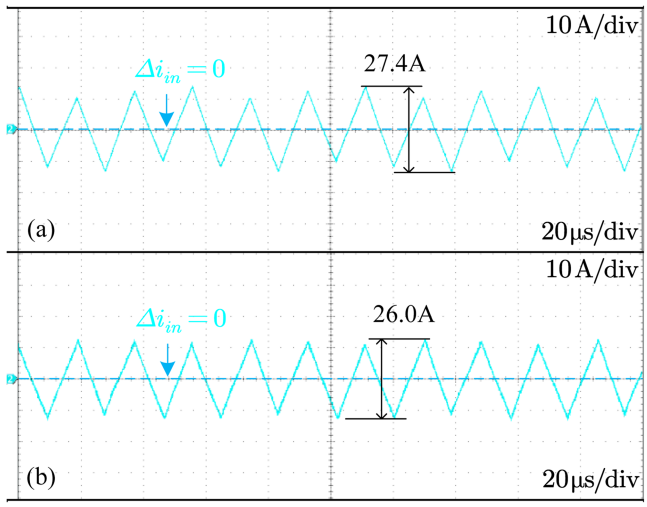

Fig. 24. Input current ripple before and after PWM phase-shift adjustment ($D_{B1} = D_{B2} = D_{B3} = 0.5$, constant voltage load): (a) using default phase shift; (b) using adjusted phase shift.

C. Experimental Verification of Transient Performance Analysis for MCCI

1) Transient Experiment Under Common-Mode Duty Cycle Perturbation: According to the analysis in Section II, when the same cycle-averaged voltage perturbation is applied to each phase of the coupled-inductance multiphase converter, the equivalent transient inductance of each of its phase is equal to the pseudodecoupled inductance. In this experiment, the converter was operated under the three-phase operation mode of phase B1, phase B2, and phase B3, with the resistive load. The PWM phase shift of each phase differs by $2\pi/3$ in turn, and the duty cycle of each phase was set to 0.5. Then, an increment of 0.1 is applied to the PWM duty cycle of each phase. The current and voltage waveforms are shown in Fig. 22. The experimental results and the theoretical transient inductance are shown in Table VII(c), where the theoretical transient inductance values are the pseudodecoupled inductance values in Table VI.

Comparing the experimental transient inductances and the theoretical transient inductances shown in Table VII(c), it can be found that they are very close, which verifies the theoretical analysis in Section II.

2) Transient Experiment Under Differential Mode Duty Cycle Perturbation: Section II provides the formulas for calculating the differential mode equivalent transient inductance matrix. In this experiment, the converter was operated under the three-phase operation mode of phase B1, phase B2, and phase B3, with the resistive load. The PWM phase shift of each phase differs by $2\pi/3$ in turn, and the duty cycle of each phase was set to 0.5. Then an increment of 0.1 is applied to the PWM duty cycle of phase B1. The current and voltage waveforms are shown in Fig. 23. The experimental results and the theoretical differential mode transient inductances calculated according to (21) and (22) are shown in Table VII(d).

The difference between the experimental results and theoretical calculations under this experimental condition is not significant, which validates the theoretical analysis of the differential mode transient behavior in Section II.

D. Experimental Verification of PWM Phase-Shift and Phase-Sequence Adjustment Methods for MCACI

1) Experimental Verification of PWM Phase-Shift Adjustment Method: Section IV analyzes the PWM phase-shift optimization strategy for MCACI. In this experiment, the converter was operated under the three-phase operation mode of phase B1, phase B2, and phase B3, with the constant voltage load. The PWM phase-shift strategies are shown in Table II, and the duty cycle of each phase was set to 0.5. The input current ripple waveforms are shown in Fig. 24, and the experimental results are shown in Table VII(e). After using the adjusted phase-shift strategy, the peak-to-peak value of the input current ripple of the converter is reduced by 5.1% compared to the default strategy. This indicates that adjusting the phase shift can reduce the input current ripple, verifying the theoretical analysis of the phase shift adjustment method of MCCI in Section IV.

2) Experimental Verification of PWM Phase Sequence Adjustment Method: Section IV analyzes the PWM sequence optimization strategy for MCCI. In this experiment, the converter was operated under the six-phase operation mode, with the constant voltage load. The PWM phase shift of each phase differs by $2\pi/3$ in turn, and the duty cycle of each phase was set to 0.5. The PWM phase sequence strategies are shown in Table III. The input current ripple waveforms are shown in Fig. 25, and the experimental results are shown in Table VII(f). After using the optimized phase sequence strategy, the peak-to-peak value of input current ripple of the converter was reduced by 79.9% compared to the default phase sequence and reduced by 22.4% compared to the empirical phase sequence. This indicates that adjusting the phase sequence can reduce the input current ripple, verifying the theoretical analysis of the phase sequence adjustment method of MCCI in Section IV.

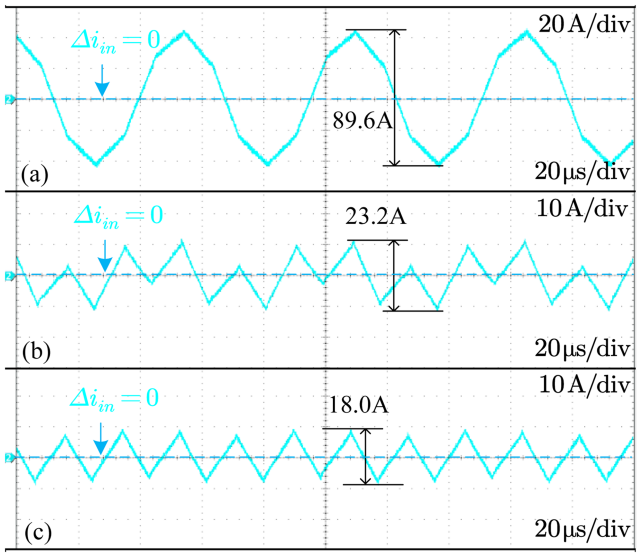

Fig. 25. Input current ripple at different PWM phase sequences ($D_{A1} = D_{A2} = D_{A3} = D_{B1} = D_{B2} = D_{B3} = 0.5$, constant voltage load): (a) using default phase sequence; (b) using empirical phase sequence; (c) using optimized phase sequence.

VI. Conclusion

This article presents a comprehensive study of the novel generalized modeling method of MCCIs. The idea of pseudodecoupling equivalence is proposed, and the performance and PWM phase-shift and phase-sequence adjustment method of MCCI are analyzed. Furthermore, the accuracy of the modeling and analysis method is verified through simulation and experiment. This provides a strong theoretical foundation for deploying coupled inductors in high-power multiphase converters, as well as a novel approach and methodology for designing high-power multiphase converters. Future research should concentrate on the performance characteristics of MCCI under DCM conditions. Moreover, in addition to the optimal control of phase shift and phase sequence, other MCCI control strategies can be considered for the design of MCCI using the present modeling approach.

Appendix A
Proof of (8)

Suppose $\mathbf{V_{dp}} = \mathbf{V_{cp}} = \mathbf{V}$, and the elements of the voltage vector $\mathbf{V}$ are equal. If V_i denotes the ith element of the vector $\mathbf{V}$, i.e., when $V_1 = V_2 = \cdots = V_n = v$, then

$$\mathbf{V} = v\mathbf{p}. \tag{93}$$

Substituting into (1) gives

$$v\mathbf{p} = \mathbf{L}\mathbf{I_{cp}}. \tag{94}$$

Since the inductance matrices in practice must be strictly diagonal dominant matrices, the matrix $\mathbf{L}$ is invertible, and we have

$$v\mathbf{L}^{-1}\mathbf{p} = \mathbf{I_{cp}}. \tag{95}$$

Denote by $\mathbf{L}^{-1}\mathbf{p}(i)$ the *i*th element of the n-dimensional vector $\mathbf{L}^{-1}\mathbf{p}$. Denote by $\mathbf{I_{cp}}(i)$ the *i*th element of the *n*-dimensional vector $\mathbf{I_{cp}}$. The above equation can be written in the form of a linear equation

$$\begin{cases} v\mathbf{L}^{-1}\mathbf{p}(1) = \mathbf{I_{cp}}(1) \\ v\mathbf{L}^{-1}\mathbf{p}(2) = \mathbf{I_{cp}}(2) \\ \quad\vdots \\ v\mathbf{L}^{-1}\mathbf{p}(n) = \mathbf{I_{cp}}(n) \end{cases}. \tag{96}$$

Since $V_1 = V_2 = \ldots = V_n = v$, there is

$$\begin{cases} V_1 = 1/\mathbf{L}^{-1}\mathbf{p}(1) \cdot \mathbf{I_{cp}}(1) \\ V_2 = 1/\mathbf{L}^{-1}\mathbf{p}(2) \cdot \mathbf{I_{cp}}(2) \\ \quad\vdots \\ V_n = 1/\mathbf{L}^{-1}\mathbf{p}(n) \cdot \mathbf{I_{cp}}(n) \end{cases}. \tag{97}$$

The linear equation can be expressed in matrix form

$$\underbrace{\begin{bmatrix} V_1 \\ V_2 \\ \vdots \\ V_n \end{bmatrix}}_{\mathbf{V}} = \underbrace{\begin{bmatrix} \frac{1}{\mathbf{L}^{-1}\mathbf{p}(1)} & & & \\ & \frac{1}{\mathbf{L}^{-1}\mathbf{p}(2)} & & \\ & & \ddots & \\ & & & \frac{1}{\mathbf{L}^{-1}\mathbf{p}(n)} \end{bmatrix}}_{\mathrm{diag}(\mathbf{L}^{-1}\mathbf{p})^{-1}} \underbrace{\begin{bmatrix} di_{\mathrm{cp}_1}/dt \\ di_{\mathrm{cp}_2}/dt \\ \vdots \\ di_{\mathrm{cp}_n}/dt \end{bmatrix}}_{\mathbf{I_{cp}}}. \tag{98}$$

That is $\mathbf{V} = \mathbf{L_{dp}}\mathbf{I_{cp}}$, which completes the proof of (8).

Appendix B
Definition of the Phase Sequence Strategy Optimization Problem

A. Variable Definitions and Constraints

The *n*-dimensional vector $\mathbf{x}$ represents the phase sequence. Denote by x_i the *i*th element of the vector $\mathbf{x}$. The phase sequence vector $\mathbf{x}$ is an arrangement of the set $\{1, 2, \ldots, n\}$ with $x_1 = 1$.

Define the *n*-dimensional phase-shift vector $\boldsymbol{\theta}$, and denote by θ_i the *i*th element of the vector $\boldsymbol{\theta}$. If we analyze the effect of the phase sequence under the condition that the phases differ sequentially by $2\pi/n$, we have

$$\theta_i = \frac{2(i-1)\pi}{n}. \tag{99}$$

Define the *n*-dimensional duty cycle vector $\mathbf{D}$. Denote the *j*th element of the vector $\mathbf{D}$ by D_j. D_j is the duty cycle of the *j*th phase in the order of the inductor layout of the converter.

L_{dp_j} is the *j*th phase pseudodecoupled inductance in the order of the converter inductor layout.

B. Objective Function

1) Objective Function Constructed With the Current Ripple Equation: With the phase-shift vector $\boldsymbol{\theta}$ and duty cycle vector $\mathbf{D}$ set, the optimal phase sequence $\mathbf{x}$ can be found by minimizing the ripples at the PCC for an MCACI with pseudodecoupled inductance matrix $\mathbf{L_{dp}}$. According to (32), the peak-to-peak value $I_{\mathrm{P2P}}(\mathbf{x}, \mathbf{D}, \boldsymbol{\theta})$ of the current ripple at the PCC at this point

is

$$I_{\mathrm{P2P}}(\mathbf{x},\mathbf{D},\boldsymbol{\theta}) = \max_{k=1}^{n}\left\{\Delta i_{(\mathbf{x},\mathbf{D},\boldsymbol{\theta})}\left(\frac{\theta_k}{2\pi}T_{\mathrm{sw}}\right),\Delta i_{(\mathbf{x},\mathbf{D},\boldsymbol{\theta})}\left(\frac{\theta_k}{2\pi}T_{\mathrm{sw}}+D_{x_k}T_{\mathrm{sw}}\right)\right\} - \min_{k=1}^{n}\left\{\Delta i_{(\mathbf{x},\mathbf{D},\boldsymbol{\theta})}\left(\frac{\theta_k}{2\pi}T_{\mathrm{sw}}\right),\Delta i_{(\mathbf{x},\mathbf{D},\boldsymbol{\theta})}\left(\frac{\theta_k}{2\pi}T_{\mathrm{sw}}+D_{x_k}T_{\mathrm{sw}}\right)\right\} \tag{100}$$

where

$$\Delta i_{(\mathbf{x},\mathbf{D},\boldsymbol{\theta})}(t) = \frac{V_{\mathrm{h}}}{f_{\mathrm{sw}}}\sum_{j=1}^{n}\frac{D_{x_j}}{L_{\mathrm{dp}_{x_j}}}f_{x_j}\left(t-\frac{\theta_j}{2\pi}T_{\mathrm{sw}}\right). \tag{101}$$

If the duty cycle of each phase is uniform $\bar{D}$, the optimal phase sequence $\mathbf{x}$ of the duty cycle interval $[lD, uD]$ is required, and the objective function can be set as

$$\int_{lD}^{uD} I_{\mathrm{P2P}}\left(\mathbf{x},\bar{D},\boldsymbol{\theta}\right)d\bar{D}. \tag{102}$$

2) Simplified Objective Function: The objective function can be simplified by using the method of summing the fundamental waveform phasors. If the duty cycle of each phase is uniform $\bar{D}$, the optimal phase sequence $\mathbf{x}$ of the duty cycle interval $[lD, uD]$ is required, and the objective function can be set as

$$\int_{lD}^{uD} P_{\mathrm{sum}}\left(\mathbf{x},\bar{D},\boldsymbol{\theta}\right)d\bar{D} \tag{103}$$

where

$$P_{\mathrm{sum}}\left(\mathbf{x},\mathbf{D},\boldsymbol{\theta}\right) = \left|\sum_{i=1}^{n}A_{x_i}e^{i\theta_i}\right|, \tag{104}$$

$$A_{x_i} = \frac{2V_{\mathrm{h}}}{L_{\mathrm{dp}_{x_i}}\left(1-D_{x_i}\right)\pi^2}\sin\left(D_{x_i}\pi\right). \tag{105}$$

ACKNOWLEDGMENT

The authors would like to thank Prof. Jose I. Leon from Universidad de Sevilla (US) in Spain for his valuable suggestions on improving the manuscript. They also would like to thank Mr. Shibo Zhang and Mr. Weijun Han for their constructive discussion in this research work and for providing the test dc–dc converter.

REFERENCES

[1] J. Dadkhah, C. N. M. Ho, K. K.-M. Siu, and R. T.-H. Li, "Magnetic components reduction in a three-phase PFC converter by using a reconfigurable LCL filter," *IEEE Trans. Power Electron.*, vol. 37, no. 12, pp. 14926–14943, Dec. 2022, doi: 10.1109/TPEL.2022.3189203.

[2] J. Ebrahimi, O. Salari, S. Eren, K. Hashtrudi-Zaad, A. Bakhshai, and P. Jain, "Efficiency improved multi-source inverter for hybrid energy storage systems in electric vehicle application," *IEEE Trans. Power Electron.*, vol. 37, no. 2, pp. 1982–1997, Feb. 2022, doi: 10.1109/TPEL.2021.3104759.

[3] S. Arab Ansari, J. N. Davidson, and M. P. Foster, "Fully-integrated planar transformer with a segmental shunt for LLC resonant converters," *IEEE Trans. Ind. Electron.*, vol. 69, no. 9, pp. 9145–9154, Sep. 2022, doi: 10.1109/TIE.2021.3116574.

[4] J. Gupta and B. Singh, "Bridgeless isolated positive output luo converter based high power factor single stage charging solution for light electric vehicles," *IEEE Trans. Ind. Appl.*, vol. 58, no. 1, pp. 732–741, Jan. 2022, doi: 10.1109/TIA.2021.3131647.

[5] J. W. Kolar et al., "PWM converter power density barriers," in *Proc. 2007 Power Convers. Conf.–Nagoya*, Apr. 2007, pp. P-9–P-29, doi: 10.1109/PCCON.2007.372914.

[6] C. R. Sullivan and M. Chen, "Coupled inductors for fast-response high-density power delivery: Discrete and integrated," in *Proc. 2021 IEEE Custom Integr. Circuits Conf.*, Apr. 2021, pp. 1–8. doi: 10.1109/CICC51472.2021.9431437.

[7] F. Zhu and Q. Li, "Coupled inductors with an adaptive coupling coefficient for multiphase voltage regulators," *IEEE Trans. Power Electron.*, vol. 38, no. 1, pp. 739–749, Jan. 2023, doi: 10.1109/TPEL.2022.3203855.

[8] M. Li, Y. Liu, Z. Ouyang, and M. A. E. Andersen, "Butterfly interleaving winding arrangements for multiphase coupled inductors," *IEEE Trans. Power Electron.*, vol. 38, no. 3, pp. 3315–3327, Mar. 2023, doi: 10.1109/TPEL.2022.3220593.

[9] P. Zumel, O. García, J. A. Cobos, and J. Uceda, "Tight magnetic coupling in multiphase interleaved converters based on simple transformers," in *Proc. 20th Annu. IEEE Appl. Power Electron. Conf. Expo.*, Mar. 2005, vol. 1, pp. 385–391, doi: 10.1109/APEC.2005.1452960.

[10] J. Li, A. Stratakos, C. R. Sullivan, and A. Schultz, "Using coupled inductors to enhance transient performance of multi-phase buck converters," in *Proc. 19th Annu. IEEE Appl. Power Electron. Conf. Expo.*, 2004, vol. 2, pp. 1289–1293, doi: 10.1109/APEC.2004.1295989.

[11] A. M. Schultz and C. R. Sullivan, "Voltage converter with coupled inductive windings, and associated methods," U.S. Patent 6,362,986, Mar. 26, 2002.

[12] D. P. Jovanovic, M. A. H. Broadmeadow, R. R. Taylor, G. R. Walker, and G. F. Ledwich, "Decoupling of current balancing and reference tracking control in parallel interleaved converters," *IEEE Trans. Power Electron.*, vol. 35, no. 4, pp. 4286–4295, Apr. 2020, doi: 10.1109/TPEL.2019.2936858.

[13] J. Imaoka et al., "A magnetic design method considering DC-Biased magnetization for integrated magnetic components used in multiphase boost converters," *IEEE Trans. Power Electron.*, vol. 33, no. 4, pp. 3346–3362, Apr. 2018, doi: 10.1109/TPEL.2017.2707385.

[14] F. Zhu, X. Lou, and Q. Li, "An improved hybrid-coupled inductor structure with flux reduction and integrated controllable coupling function," *IEEE Trans. Power Electron.*, vol. 39, no. 1, pp. 1103–1114, Jan. 2024, doi: 10.1109/TPEL.2023.3294471.

[15] L. Wang, D. Zhang, and L. Lyu, "A novel array-type symmetrical CI for multiphase interleaved DC–DC converters," *IEEE J. Emerg. Sel. Top. Power Electron.*, vol. 10, no. 5, pp. 5969–5986, Oct. 2022, doi: 10.1109/JESTPE.2022.3164329.

[16] W. Huang and B. Lehman, "Inversely coupled inductors with small volume and reduced power loss for switching converters," *IEEE Trans. Power Electron.*, vol. 38, no. 6, pp. 6779–6783, Jun. 2023, doi: 10.1109/TPEL.2023.3241883.

[17] P. L. Wong, P. Xu, B. Yang, and F. C. Lee, "Performance improvements of interleaving VRMs with coupling inductors," *IEEE Trans. Power Electron.*, vol. 16, no. 4, pp. 499–507, Jul. 2001, doi: 10.1109/63.931059.

[18] Y. Dong, "Investigation of multiphase coupled-inductor buck converters in point-of-load applications," PhD Thesis, Virginia Tech, 2009.

[19] Y. Yang, Y. Wu, X. Sun, and X. Han, "Design criterion and guidelines for three-phase asymmetric coupled inductors in interleaving DC/DC converter for VRM in data centres and POL," *IET Power Electron.*, vol. 13, no. 13, pp. 2854–2865, 2020, doi: 10.1049/iet–pel.2019.1451.

[20] D. Zhou, Y. Elasser, J. Baek, and M. Chen, "Reluctance-based dynamic models for multiphase coupled inductor buck converters," *IEEE Trans. Power Electron.*, vol. 37, no. 2, pp. 1334–1351, Feb. 2022, doi: 10.1109/TPEL.2021.3105085.

[21] M. Chen and C. R. Sullivan, "Unified models for coupled inductors applied to multiphase PWM converters," *IEEE Trans. Power Electron.*, vol. 36, no. 12, pp. 14155–14174, Dec. 2021, doi: 10.1109/TPEL.2021.3088083.

[22] J. Li, C. R. Sullivan, and A. Schultz, "Coupled-inductor design optimization for fast-response low-voltage DC-DC converters," in *Proc. APEC. 17th Annu. IEEE Appl. Power Electron. Conf. Expo. (Cat. No.02CH37335)*, Mar. 2002, vol. 2, pp. 817–823, doi: 10.1109/APEC.2002.989338.

[23] R. A. Ali, M. Shousha, and M. Haug, "Generalized automated tool for analysis and design of multiphase coupled inductor buck converters," in *Proc. 24th Eur. Conf. Power Electron. Appl. (EPE'22 ECCE Europe)*, Sep. 2022, pp. 1–11.

[24] J. Zhang et al., "Lifetime extension approach based on the levenberg–marquardt neural network and power routing of DC–DC converters," *IEEE Trans. Power Electron.*, vol. 38, no. 8, pp. 10280–10291, Aug. 2023, doi: 10.1109/TPEL.2023.3275791.
[25] V. G. Monopoli et al., "A hybrid modulation technique for operating medium-voltage high-power CHB converters under grid voltage disturbances," *IEEE Trans. Ind. Electron.*, vol. 71, no. 1, pp. 462–472, Jan. 2024, doi: 10.1109/TIE.2023.3241246.
[26] O. Garcia, A. de Castro, P. Zumelis, and J. A. Cobos, "Digital-control-based solution to the effect of nonidealities of the inductors in multiphase converters," *IEEE Trans. Power Electron.*, vol. 22, no. 6, pp. 2155–2163, Nov. 2007, doi: 10.1109/TPEL.2007.909406.
[27] M. L. A. Caris, H. Huisman, J. M. Schellekens, and J. L. Duarte, "Generalized harmonic elimination method for interleaved power amplifiers," in *Proc. IECON 2012-38th Annu. Conf. IEEE Ind. Electron. Soc.*, Oct. 2012, pp. 4979–4984, doi: 10.1109/IECON.2012.6388985.
[28] M. L. A. Caris, H. Huisman, and J. L. Duarte, "Harmonic elimination by adaptive phase-shift optimization in interleaved converters," in *Proc. 2013 IEEE Energy Convers. Congr. Expo.*, Sep. 2013, pp. 763–768, doi: 10.1109/ECCE.2013.6646779.
[29] D. Zhan, L. Wei, Y. Zhang, and Y. Yao, "A generalized model of nonisolated multiphase DC-DC converter based on novel switching period averaging method," *IEEE Trans. Power Electron.*, vol. 30, no. 9, pp. 5181–5191, Sep. 2015, doi: 10.1109/TPEL.2014.2361019.
[30] P. Wang, D. H. Zhou, Y. Elasser, J. Baek, and M. Chen, "Matrix coupled all-in-one magnetics for PWM power conversion," *IEEE Trans. Power Electron.*, vol. 37, no. 12, pp. 15035–15050, Dec. 2022, doi: 10.1109/TPEL.2022.3194418.
[31] B. Miwa, "Interleaved conversion techniques for high density power supplies," PhD Thesis, Massachusetts Inst. Technol., Cambridge, MA, USA, 1992.
[32] Z. Yao et al., "Nonlinear inductor–based single sensor current balancing method for interleaved DC–DC converters," *IEEE Trans. Power Electron.*, vol. 39, no. 4, pp. 3996–4000, Apr. 2024, doi: 10.1109/TPEL.2024.3355281.

Li Wei (Member, IEEE) received the B.S. degree in electrical engineering and the Ph.D. degree in control theory and control engineering from Tongji University, Shanghai, China, in 2004 and 2010, respectively.

Since 2000, she has been with Tongji University, where she is currently an Associate Professor in electrical engineering with the School of Electronics and Information Engineering. From 2007 to 2008, she was a Visiting Ph.D. Student with Ecole des Mines de Paris, Sophia Antipolis, France. From 2014 to 2015, she was a Visiting Scientist with RWTH Aachen University, Aachen, Germany. In 2019, she was a Visiting Scientist with Aalborg University, Aalborg, Denmark. Her current research interests include high-power density dc/dc converter for fuel cell vehicle and energy storage application.

Dr. Wei was the recipient of the Green Talents Award from the German Federal Ministry of Education and Research, in 2014.

Bingqi Ouyang (Member, IEEE) received the B.S. degree in electrical engineering and automation from Donghua University, Shanghai, China, in 2021, and the M.S. degree in electrical engineering from Tongji University, Shanghai, China, in 2024.

Her research interests include integrated magnetic components, high-density power conversion systems, and power electronic converter modeling and control techniques.

Yanbo Liu (Graduate Student Member, IEEE) received the B.S. degree in electrical engineering and automation in 2022 from Tongji University, Shanghai, China, where he is currently working toward the M.S. degree in electrical engineering with the Department of Electrical Engineering.

His research interests include integrated magnetic components and onboard power electronic converters.